An ultra-short period super-Earth and sub-Neptune spanning the Radius Valley orbiting the kinematic thick disc star TOI-2345

Monthly Notices of the ROYAL ASTRONOMICAL SOCIETY

MNRAS **544,** 2614–2636 (2025) https://doi.org/10.1093/mnras/staf1806
Advance Access publication 2025 October 20

An ultra-short period super-Earth and sub-Neptune spanning the Radius Valley orbiting the kinematic thick disc star TOI-2345

Yoshi Nike Emilia Eschen [1★] Thomas G. Wilson [1] Andrea Bonfanti [2] Carina M. Persson,[3] Sérgio G. Sousa [4] Monika Lendl [5] Alexis Heitzmann [5] Attila E. Simon [6,7] Göran Olofsson [8] Amadeo Castro-González,[5] Jo Ann Egger [6] Luca Fossati [2] Alexander James Mustill [9] Hugh P. Osborn [7,10] Hugo G. Vivien [11] Yann Alibert [7,6] Roi Alonso [12,13] Tamas Bárczy [14] David Barrado [15] Susana C. C. Barros [4,16] Wolfgang Baumjohann [2] Willy Benz [6,7] Nicolas Billot [5] Luca Borsato [17] Alexis Brandeker [8] Christopher Broeg [6,7] Maximilian Buder,[18] Douglas A. Caldwell [19] Andrew Collier Cameron [20] Alexandre C. M. Correia [21] Szilard Csizmadia [18] Patricio E. Cubillos,[2,22] Melvyn B. Davies [23] Magali Deleuil [11] Adrien Deline,[5] Olivier D. S. Demangeon [4,16] Brice-Olivier Demory [7,24,6] Aliz Derekas,[25] Billy Edwards,[26] David Ehrenreich [5,27] Anders Erikson,[18] Jacopo Farinato [17] Andrea Fortier [6,7] Malcolm Fridlund [28,3] Davide Gandolfi [29] Kosmas Gazeas [30] Michaël Gillon [31] Robert Goeke,[32] Manuel Güdel,[33] Maximilian N. Günther [34] Johann Hasiba,[2] Ch. Helling,[2,35] Kate G. Isaak [34] Jon M. Jenkins,[36] Tatiana Keller,[6,7] Laszlo L. Kiss,[37,38] Daniel Kitzmann,[6,7] Judith Korth [5] Kristine W. F. Lam [18] Jacques Laskar [39] Alain Lecavelier des Etangs [40] Adrien Leleu [5,6] Demetrio Magrin [17] Pierre F. L. Maxted [41] Bruno Merín [42] Christoph Mordasini,[6,7] Valerio Nascimbeni [17] Roland Ottensamer,[33] Isabella Pagano [43] Enric Pallé [12,13] Gisbert Peter [18] Daniele Piazza,[44] Giampaolo Piotto [17,45] Don Pollacco,[1] Didier Queloz [10,46] Roberto Ragazzoni [17,45] Nicola Rando,[34] Francesco Ratti,[34] Heike Rauer [47,48] Ignasi Ribas [49,50] Nuno C. Santos [4,16] Gaetano Scandariato [43] Damien Ségransan [5] Avi Shporer,[32] Alexis M. S. Smith [18] Manu Stalport,[51,31] Sophia Sulis [11] Gyula M. Szabó [25,52] Stéphane Udry [5] Solène Ulmer-Moll [53,51] Valérie Van Grootel [51] Julia Venturini [5] Eva Villaver,[12,13] Nicholas A. Walton [54] David Watanabe,[55] Sebastian Wolf[6] and Carl Ziegler[56]

Affiliations are listed at the end of the paper

Accepted 2025 October 11. Received 2025 October 8; in original form 2025 September 9

ABSTRACT

A crucial chemical link between stars and their orbiting exoplanets is thought to exist. If universal, this connection could affect the formation and evolution of all planets. Therefore, this potential vital link needs testing by characterizing exoplanets around chemically-diverse stars. We present the discovery of two planets orbiting the metal-poor, kinematic thick-disc K-dwarf TOI-2345. TOI-2345 b is a super-Earth with a period of 1.05 d and TOI-2345 c is a sub-Neptune with a period of 21 d. In addition to the target being observed in four *TESS* sectors, we obtained five *CHEOPS* visits and 26 radial velocities from HARPS. By conducting a joint analysis of all the data, we find TOI-2345 b to have a radius of $1.504^{+0.047}_{-0.044}\,R_\oplus$ and a mass of $3.49 \pm 0.85\,M_\oplus$; and TOI-2345 c to have a radius of $2.451^{+0.045}_{-0.046}\,R_\oplus$ and a mass of $7.27^{+2.27}_{-2.45}\,M_\oplus$. To explore chemical links between these planets and their host star, we model their interior structures newly accounting for devolatized stellar abundances. TOI-2345 adds to the limited sample of well-characterized planetary systems around thick disc stars. This system challenges theories of formation and populations of planets around thick disc stars with its Ultra-Short Period super-Earth and the wide period distribution of these two planets spanning the radius valley.

★ E-mail: yoshi.eschen@warwick.ac.uk

Key words: techniques: photometric - techniques: radial velocities – planets and satellites: detection – planets and satellites: interiors – planets and satellites: individual: TOI-2345 b & c – stars: individual: TOI-2345.

1 INTRODUCTION

Since the discovery of the first exoplanet orbiting a main sequence star, 51 Peg (M. Mayor & D. Queloz 1995), the field has been exponentially growing. Beginning with radial velocity (RV) surveys in the late 1990s and early 2000s (e.g. D. Queloz et al. 2000; N. C. Santos et al. 2004) a few hundreds of exoplanets were detected, the majority of which are of high masses such as Jupiter. During the last decades instruments such as High Accuracy Radial Velocity Planet Searcher (HARPS; F. Pepe et al. 2000; M. Mayor et al. 2003), ESPRESSO (F. Pepe et al. 2021) or EXPRES (C. Jurgenson et al. 2016) obtaining higher precisions, as well as our ability to model stellar activity, has opened the door to measure smaller mass planets down to that of Earth (e.g. J. I. González Hernández et al. 2024; D. A. Turner et al. 2025). However, the main increase in the number of exoplanet detections over the last 15 yr was due to space-based photometric missions detecting transiting planets and deriving their radii. NASA's *Kepler* mission (W. J. Borucki et al. 2010) observed a fixed field in the Northern Hemisphere from 2009 to 2013. This mission discovered nearly 3000 confirmed and validated planets (NASA Exoplanet Archive 2025, accessed on 2025 July 17). After the failure of two of the four reaction wheels the *Kepler* mission was continued as *K2* (S. B. Howell et al. 2014) observing several fields around the ecliptic until 2018, adding to the sample of transiting planets. Since 2018, NASA's *Transiting Exoplanet Survey Satellite* (*TESS*; G. R. Ricker et al. 2015) has been performing an all-sky survey and has detected 643 planets to date (NASA Exoplanet Archive 2025, accessed on 2025 July 17). Additionally, ESA's photometric mission, *CHaracterizing ExOPlanet Satellite* (*CHEOPS*; W. Benz et al. 2021), is following up discovered transiting planets and planet candidates to derive their radii more precisely. By the end of 2026, ESA's upcoming *PLAnetary Transits and Oscillations* of stars mission (*PLATO*; H. Rauer et al. 2025) is expected to launch. As this mission will observe bright and nearby targets for at least two years and with up to 24 cameras, it is expected to reach higher precisions than *TESS* and *CHEOPS* allowing to better characterize transiting planets and discover further systems. *PLATO*'s long continuous observation will also enables finding planets of longer orbital periods including outer planets in known systems with short period planets (Y. N. E. Eschen et al. 2024; H. Rauer et al. 2025).

Among these newly discovered planets by *Kepler* were two planet types not found in our own Solar system: super-Earths and sub-Neptunes (N. M. Batalha et al. 2013). The large sample of *Kepler* planets allowed demographics studies with these planet types found to be the most common in our Milky Way (A. W. Howard et al. 2012; E. A. Petigura, G. W. Marcy & A. W. Howard 2013). By studying their radius distribution, a dearth of planets between $\sim$1.5–2 $R_\oplus$ was found (B. J. Fulton et al. 2017; R. Burn et al. 2024), named the radius valley. For FGK dwarfs the radius valley seems to arise from atmospheric mass-loss (V. Van Eylen et al. 2018). In addition to atmospheric escape from either photoevaporation or core-powered mass-loss (J. E. Owen & H. E. Schlichting 2024) the radius valley can also be explained by formation and evolution models (J. Venturini et al. 2020). Importantly, the radius valley is stellar mass and orbital period dependent (C. S. K. Ho & V. Van Eylen 2023). However, not many multiplanetary systems that span the valley, especially at long orbital periods, have been studied. Hence these systems remain exciting to study and provide insights into planet formation and evolution processes.

Below the radius valley lie super-Earths. Within this sample, a population of Ultra-Short Period (USP) planets have been discovered (R. Sanchis-Ojeda et al. 2014; E. R. Adams et al. 2021). These are planets that orbit their host star in less than or roughly 1 d (A. V. Goyal & S. Wang 2025) and are hence highly irradiated. Therefore they have likely lost their atmospheres and can provide insights into the deeper interior of small planets (J. N. Winn et al. 2017; F. Dai et al. 2019). Since several hundreds of these planets have been found to date (NASA Exoplanet Archive 2025, accessed on 17 July 2025), they have been part of several demographics studies (J. N. Winn, R. Sanchis-Ojeda & S. Rappaport 2018). These include the findings of F. Dai, K. Masuda & J. N. Winn (2018) reporting that USPs have higher mutual inclinations than other systems. P.-W. Tu et al. (2025) found that USPs are more often found around older thick disc stars and the period spacings between them and outer bodies seem to increase with age. Since their origin and evolution is still not fully understood they remain interesting planets to characterize. Overall, the origin and evolution of USPs is not fully understood, even though it is commonly thought that these planets migrated inwards through interactions with outer companions (e.g. C. Petrovich, E. Deibert & Y. Wu 2019; B. Pu & D. Lai 2019; S. C. Millholland & C. Spalding 2020).

Since the planetary radius and orbital inclination can be derived from the photometric data and the mass multiplied by the inclination from RV observations, combining the two methods is valuable to characterize systems well. Knowing the bulk density of small planets (in this context $R_P < 4\,R_\oplus$) allows modelling of their interior structure (C. Huang, D. R. Rice & J. H. Steffen 2022; P. Baumeister & N. Tosi 2023; J. A. Egger et al. 2024). This provides insight into planet formation and evolution mechanisms such as core accretion and atmospheric escape (J. E. Owen & R. Murray-Clay 2018; P. J. Armitage 2020; D. Kubyshkina & L. Fossati 2022). As found by V. Adibekyan et al. (2021), T. G. Wilson et al. (2022), V. Adibekyan et al. (2024) there may be a compositional link between the host star abundances and the interior structure of these planets since they are formed from the same material and the abundances are unlikely to have changed significantly during the formation (A. Thiabaud et al. 2015; J. Nielsen et al. 2023; J. H. Steffen et al. 2025) as seen by the abundances of refractory elements in the proto-Sun and Earth (H. S. Wang, C. H. Lineweaver & T. R. Ireland 2019a).

However, there is a lack of planets around metal-poor and α-enhanced stars which is not clear if it arises from physical or observational origin. Hence to identify trends linking stellar and planetary composition, and perform demographic studies, this sample needs to be increased. Metal-poor and α-enhanced stars are most likely to be found in the kinematic thick disc of the Milky Way (K. Fuhrmann 1998; M. R. Hayden et al. 2015). This is due to the Interstellar Medium (ISM) being enriched in α-elements due to more massive stars ($M > 8\,M_\odot$) exploding in type II supernova at the earlier stages of the Milky Way. With more time low-mass stars evolved into white dwarfs and type Ia supernova could enrich the ISM with iron-peak elements (J. C. Wheeler, C. Sneden & J. W. Truran 1989; P. Gondoin 2024; J. H. Steffen et al. 2025). Hence stars in the thin disc are found to be metal-rich while stars in the thick disc mainly remain metal-poor (M. R. Hayden et al. 2015). Hence, to add to the sample of small transiting planets around metal-poor stars, we characterize

the planets orbiting the kinematic thick disc star TOI-2345 hosting an USP and a sub-Neptune spanning the radius valley.

We present the data we took with *TESS*, *CHEOPS*, and HARPS to discover and characterize this system as well as the ground-based photometry and imaging in Section 2, characterize the host star properties in Section 3, model the planetary parameters in Section 4 and discuss its internal structure, atmospheric evolution and place it in the context of other thick disc stars orbited by super-Earths and sub-Neptunes in Section 5. Finally, we conclude in Section 6.

2 OBSERVATIONS

In order to characterize the TOI-2345 system, it was observed with photometric surveys including *TESS*, *CHEOPS*, ASAS-SN, and WASP; spectroscopy from HARPS and imaging observations from SOAR.

2.1 *TESS*

The Transiting Exoplanet Survey Satellite (*TESS*; G. R. Ricker et al. 2015) has been performing an all-sky survey since 2018. *TESS* consists of four cameras each containing four CCDs. To cover the entire sky it divided it up into sectors which are each observed for 27.4 d. Since its launch, it has identified 7655 planet candidates and discovered 643 new planets (NASA Exoplanet Archive 2025, accessed on 2025 July 17). Being at the end of its second extended mission now, *TESS* has changed the cadence at which it is observing targets from the original 30 mins in the prime mission, 10 mins during the first extension, and finally the current 200s cadence. Additionally, *TESS* observes selected targets at a cadence of 2 min during the primary mission and 20 s during the extensions.

TESS data is downlinked every 13.7 d. The data are processed by the Science Processing Operations Centre (SPOC; J. M. Jenkins et al. 2016; D. A. Caldwell et al. 2020) into light curves following the procedures of the *Kepler* pipeline (J. M. Jenkins et al. 2010). The produced light curves contain flux values obtained from Simple Aperture Photometry (SAP; J. D. Twicken et al. 2010b; R. L. Morris et al. 2020) as well as the Pre-search Data Conditioning SAP (PDCSAP; J. D. Twicken et al. 2010a; J. C. Smith et al. 2012; M. C. Stumpe et al. 2012), which is the SAP flux detrended using Co-trending Basis Vectors and hence showing less systematic trends. In these light curves the combined differential photometric precision (CDPP) over 2 h is reported (J. L. Christiansen et al. 2012).

Produced light curves by SPOC go through a several staged vetting process described in N. M. Guerrero et al. (2021). First, a search for transit like signals is conducted. Signals that occur twice or more and have a statistical significance of 7.1σ or more as well as some statistical tests pass this stage and are called Threshold Crossing Events (TCEs). To these a transit model is fitted and a summary report including several diagnostic tests gets produced. Within this step the pipeline also searched for further transits in the light curve. These data are then passed on to an automated Triage, *TESS*-ExoClass (TEC)[1] based on *Kepler*'s Robovetter (J. L. Coughlin et al. 2016; S. E. Thompson et al. 2018). Finally targets, passing these tests get vetted manually by a team of Vetters going through the produced reports. Additionally, several teams have developed independent searching and vetting tools (e.g. M. Montalto et al. 2020; D. L. Feliz et al. 2021; G. Olmschenk et al. 2021; M. Montalto 2023; Y. N. E. Eschen & M. Kunimoto 2024; M. Kunimoto et al. 2025)

[1] https://github.com/christopherburke/TESS-ExoClass

In this vetting process, two transiting planet candidates around TOI-2345, TOI-2345.01 and TOI-2345.02, were alerted. Hereafter, we refer to these planets as TOI-2345 b and c. TOI-2345 was observed during *TESS*'s Primary mission in sectors 3 and 4 (20 September 2018 to 14 November 2018) with a cadence of 30 min. The target was observed again in the first Extended Mission within which *TESS* collected data with a cadence of 10 min in sectors 30 and 31 (2020 September 23–2020 November 16). *TESS* will re-observe TOI-2345 in October 2025 and Summer 2026 according to *TESS*-POINT (C. J. Burke et al. 2020). We show and summarize the details of the currently available *TESS* observations in Fig. 1 and Table 1, respectively.

To perform our own analysis on this target, we downloaded the *TESS* SPOC High-level-science product light curves, for sectors 3, 4, 30, and 31. We removed bad quality data (QUALITY $>$ 0) points and analysed the PDCSAP flux in this study.

2.2 *CHEOPS*

The CHaracterising ExOPlanet Satellite (*CHEOPS*; W. Benz et al. 2021) is a S-class ESA mission launched in 2019. One of its goals is to follow-up known planets in order to derive their radii more precisely which supports constraining planet formation and evolution theories. While *TESS* produces Full Frame Images and makes these publicly available, *CHEOPS* produces window images which contain the observed target. Due to the nadir-locked, Sun-synchronous, low-Earth orbit of *CHEOPS*, each visit contains gaps from Earth occultation that is represented by a observational efficiency. We obtained a total of five *CHEOPS* visits within the *CHEOPS* X-Gal programme (ID: PR120054, PI: Wilson) within the Guaranteed Time Observing programme, see Fig. B1. These visits cover four transits of TOI-2345 b and one transit of TOI-2345 c and are summarized in Table 2.

In addition to the aperture photometry from the *CHEOPS* Data Reduction Pipeline (DRP; S. Hoyer et al. 2020), where we select the optimal aperture per visit based on the lowest RMS value, we used the PSF Imagette Photometric Extraction (PIPE; A. Brandeker, J. A. Patel & B. M. Morris 2024) to re-extract the *CHEOPS* photometry using PSF photometry. We fit each visit individually in PYCHEOPS (P. F. L. Maxted et al. 2023) using LMFIT (M. Newville et al. 2014) and the parameters obtained by a *TESS* only fit in JULIET (N. Espinoza, D. Kossakowski & R. Brahm 2019, See Section 4.1). Within PYCHEOPS subsets detrending vectors are fitted simultaneously with the transit model. By assessing the Bayes Factor of models containing different combinations of detrending vectors, we are able to obtain the detrending vectors of each visit. We report these selected detrending vectors in Table B1. We use the suggested detrending vectors as linear regressors in JULIET in order to decorrelate the five *CHEOPS* visits. We apply a 3σ clipping, removing outliers that are further away than 3σ from the mean of the data. This leaves us with two sets of five detrended *CHEOPS* visits each, one using aperture photometry from the DRP and one using PSF photometry from PIPE.

2.3 HARPS

We collected 26 high-resolution spectra of TOI-2345 with the High Accuracy Radial Velocity Planet Searcher (HARPS; F. Pepe et al. 2000). HARPS is a high-resolution Echelle spectrograph mounted on the ESO 3.6 m telescope in La Silla. HARPS has a wavelength range from 380 to 680 nm and a resolving power of 90,000. These observations were taken between 2023-07-01 and 2025-01-30 which we show in Fig. C1. The typical SNR of these observations at Order 50 is 33.44. These observations were taken as part of the 111.254R programme (PI: Wilson) with an exposure time of 1800 s.

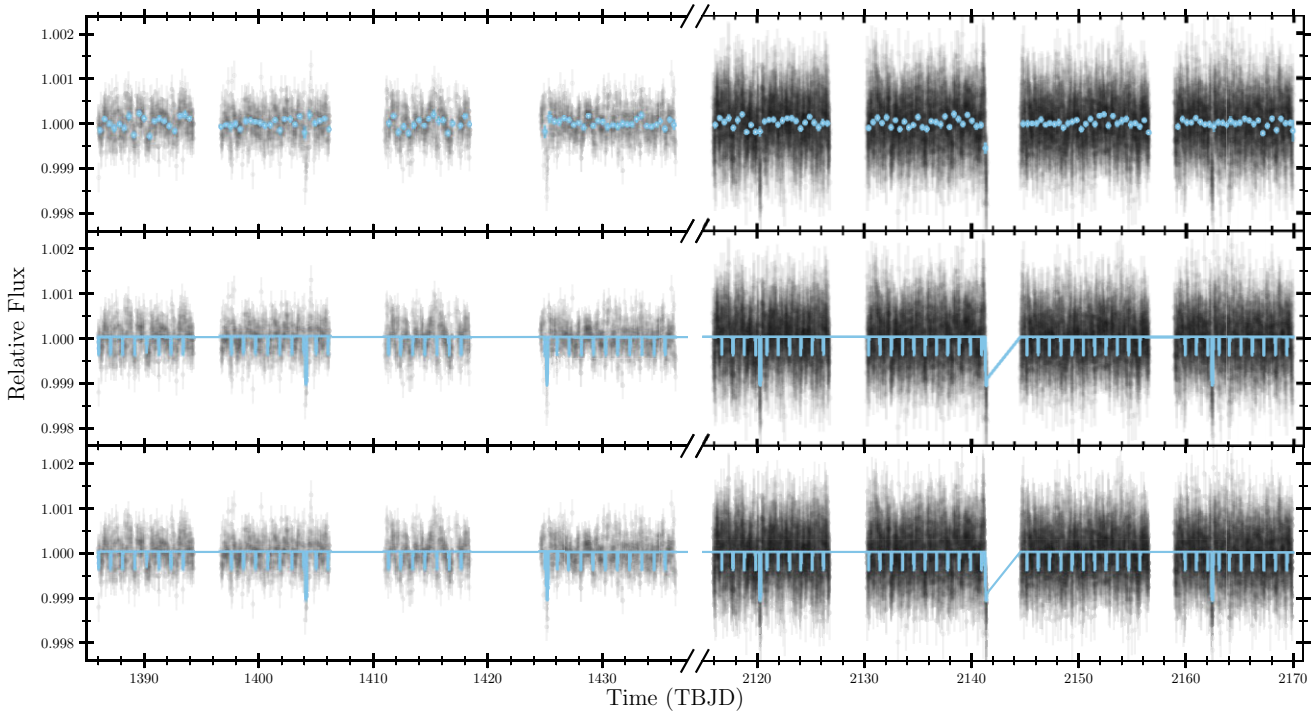

Figure 1. *TESS* data of TOI-2345 in sectors 3, 4, 30, and 31. Top: *TESS* data binned at 10 h. Middle: Transit and GP model in blue plotted on top of the data points in grey. Bottom: Transit model and *TESS* data points with the GP model subtracted.

Table 1. *TESS* observations of TOI-2345.

Sector	Camera	CCD	Start date (UTC)	End date (UTC)	Cadence (s)	2-h CDPP (ppm)	#Transits of Planet b	#Transits Planet c
3	2	2	2018-09-20T13:04:29.861	2018-10-17T21:05:07.754	1800	181.3	17	1
4	2	1	2018-10-19T10:05:08.066	2018-11-14T08:04:33.593	1800	191.2	18	1
30	2	2	2020-09-23T09:24:09.487	2020-10-20T14:34:38.274	600	200.2	21	2
31	2	1	2020-10-22T00:24:38.474	2020-11-16T10:43:57.592	600	184.6	21	1

Table 2. *CHEOPS* Observations of TOI-2345.

Visit	Planets	Start date (UTC)	Duration (h)	Data points (#)	File key	Efficiency (per cent)	Exp time (s)
1	b	2022-10-16T12:30:42	12.67	529	CH_PR120054_TG001001	71.5	60
2	c	2022-10-25T16:21:42	17.29	771	CH_PR120054_TG002401	74.2	60
3	b	2022-11-05T13:31:42	13.97	674	CH_PR120054_TG001002	80.3	60
4	b	2022-11-20T09:50:42	11.44	428	CH_PR120054_TG003201	62.3	60
5	b	2022-11-21T12:37:43	12.41	448	CH_PR120054_TG003202	60.1	60

The data were processed with the HARPS Data Reduction Software (DRS 3.2.5 C. Lovis & F. Pepe 2007). Within the DRS the RVs as well as activity indicators such as the FWHM, BIS and contrast are computed using the cross-correlation function with a K2 mask. Additionally further activity indicators, including the S, H α, Na and Ca II indices, are computed from the spectra. The HARPS RVs and activity indicators are shown in Tables C1 and C2.

As shown by A. M. Silva et al. (2022), the precision of RVs can be improved by extracting them through template matching. Hence we additionally derive RVs using Semi-Bayesian Approach for RVs with Template-matching (S-BART; A. M. Silva et al. 2022). We re-extracted the RVs using the 2D spectra from the DRS and a combination of different template-matching parameters and quality checks and compare the results to find the best combination of these. The template matching fitting parameters include RV steps of 0.1, 0.5, 1.0 m/s, RV limits of 200, 500, 1000 m s^{-1} and the classical and Laplacian method S-BART applies. As quality checks we apply minimum order SNRs of 1.5, 5, and 10, airmasses of 1.5, 2.0, 2.2 and 2.6 and RV errors of 5, 6, 7, and 10 m/s. We obtain a median error of 2.04 m s^{-1} and an RMS of 3.57 m s^{-1} when taking the median of all S-BART time series median errors and RMS. This is lower than the median error and RMS obtained from the RVs of the DRS which are 3.12 and 4.61 m s^{-1}, respectively. Since S-BART is reducing the uncertainties, we use it in the further analysis in Section 4. We describe how we select the optimal RV time series produced by S-BART from different template matching and quality parameters in Section 4.2.

2.4 ASAS-SN

The All-Sky Automated Survey for SuperNovae (ASAS-SN; B. J. Shappee et al. 2014; C. S. Kochanek et al. 2017) is photometrically monitoring the entire sky to detect transients. As this survey also monitor stars over a long time span it can be used to monitor stellar activity. TOI-2345 was observed in the ASAS-SN V band from January 2012 to September 2018 and the g band by ASAS-SN from 2017 September to 2025 August. In the 13 yr, 1062 and 5497 data points were collected for the V and g band, respectively. We apply a magnitude cut-off at $V = 15$ mag and $g = 15$ mag and 5σ clipping to this data, which removes 6 and 280 data point, leaving us with 1056 and 5217 measurements, respectively.

2.5 WASP

The Wide Angle Search for Planets (WASP; D. L. Pollacco et al. 2006) has been monitoring stars since 2004 in the Northern and Southern hemisphere to search for transiting planets. This resulted in 170 planet discoveries, of which the majority are Hot Jupiters as these have deep transits. WASP is not precise enough to detect planets as small as Earth, however its long term monitoring can be used to identify the rotation period of stars. TOI-2345 was monitored with WASP from 2006 June 17 to 2014 December 19. During this time WASP collected 12 235 data points. We remove data points with relative magnitude errors above 0.01, leaving us with 10 324 data points. Applying a 5σ clipping to the remaining data points, removes an additional two, leaving 10 322 measurements for further analysis.

2.6 Imaging

High-angular resolution imaging is needed to search for nearby sources that can contaminate the *TESS* photometry, resulting in an underestimated planetary radius, or be the source of astrophysical false positives, such as background eclipsing binaries. We searched for stellar companions to TOI-2345 with speckle imaging on the 4.1-m Southern Astrophysical Research (SOAR) telescope (A. Tokovinin 2018) on 2020 December 3 UT, observing in Cousins I band, a similar visible bandpass as *TESS*. This observation was sensitive with 5-sigma detection to a 5.0-mag fainter star at an angular distance of 1 arcsec from the target. More details of the observations within the SOAR *TESS* survey are available in C. Ziegler et al. (2020). The $5\,\sigma$ detection sensitivity and speckle autocorrelation functions from the observations are shown in Fig. 2. No nearby stars were firmly detected within 3 arcsec of TOI-2345 in the SOAR observations.

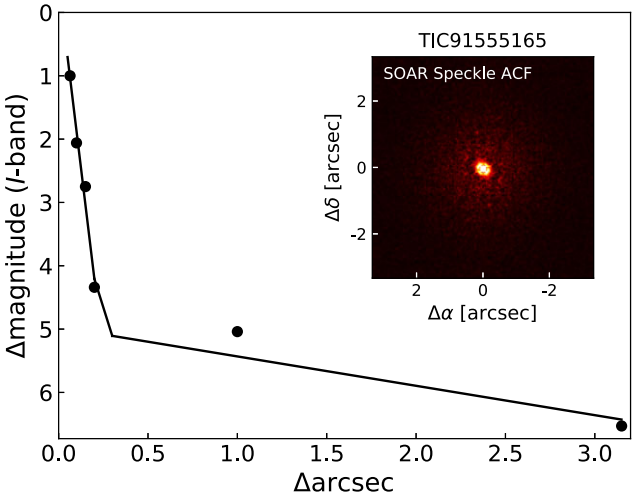

Figure 2. 5σ detection sensitivity of the SOAR I-band observation of TOI-2345.

3 STELLAR CHARACTERIZATION

3.1 Spectral analysis

We analysed the co-added high-resolution HARPS spectrum with the software Spectroscopy Made Easy[2] (SME; J. A. Valenti & N. Piskunov 1996; N. Piskunov & J. A. Valenti 2017) to obtain the stellar effective temperature ($T_{\rm eff}$), surface gravity ($\log g_\star$), and abundances ([Fe/H], [Mg/H], [Si/H]). This software fits observations to computed synthetic spectra based on a chosen stellar atmosphere grid (Atlas12; R. L. Kurucz 2013) and atomic and molecular line data from VALD (T. Ryabchikova et al. 2015). We fitted one parameter at a time following C. M. Persson et al. (2018). We fixed the micro- and macro-turbulent velocities to 0.1 km s^{-1} and 1.0 km s^{-1} and fitted a large number of iron lines to obtain the projected equatorial rotational velocity of the star ($V \sin i_\star$). The parameters derived are $T_{\rm eff} = 4687 \pm 60$ K, $\log g = 4.57 \pm 0.06$ dex, and [Fe/H] $= -0.10 \pm 0.07$ dex.

An additional independent spectral analysis was done with ARES+MOOG as described in N. C. Santos et al. (2013) and S. G. Sousa (2014, 2021). We used the latest version of ARES[3] (S. G. Sousa et al. 2007, 2015) to consistently measured the equivalent widths (EW) for the iron line list presented in S. G. Sousa et al. (2008). The best spectroscopic parameters are found using the ionization and excitation equilibrium. In this process, it is used for a grid of Kurucz model atmospheres (R. L. Kurucz 1993) and the radiative transfer code MOOG (C. A. Sneden 1973). The parameters derived ($T_{\rm eff} = 4669 \pm 122$ K, $\log g = 4.55 \pm 0.07$ dex, and [Fe/H] $= -0.11 \pm 0.05$ dex) are very consistent with the adopted values derived by SME.

3.2 Radius, mass, and age

We determined the stellar radius of TOI-2345 using a MCMC modified infrared flux method (IRFM–D. E. Blackwell & M. J. Shallis 1977; N. Schanche et al. 2020). Within this framework we constructed spectral energy distributions (SED) from two stellar atmospheric models catalogues (R. L. Kurucz 1993; F. Castelli & R. L. Kurucz 2003) constrained by our spectroscopically derived stellar parameters. To obtain the stellar bolometric flux, synthetic photometry was produced by the SEDs and compared to observed fluxes in the following bandpasses: 2MASS J, H, and K, WISE $W1$ and $W2$, and *Gaia* G, $G_{\rm BP}$, and $G_{\rm RP}$ (M. F. Skrutskie et al. 2006; E. L. Wright et al. 2010; Gaia Collaboration 2023). From the bolometric flux, we derived the effective temperature and angular diameter that was converted into the stellar radius using the offset-corrected *Gaia* parallax (L. Lindegren et al. 2021). To account for stellar atmosphere model uncertainties, we took a Bayesian Model

[2]http://www.stsci.edu/~valenti/sme.html

[3]The latest version, ARES v2, can be downloaded at https://github.com/sousasag/ARES

Table 3. Stellar properties of TOI-2345.

TOI-2345		
2MASS	J02553208-3458391	
Gaia DR3	5049575943053753088	
TIC	91555165	
LP	942-63	
Parameter	Value	Note
α [J2000]	$02^h55^m32.10^s$	1
δ [J2000]	$-34°58'39.09''$	1
μ_α [mas yr^{-1}]	202.481±0.011	1
μ_δ [mas yr^{-1}]	−104.354±0.014	1
ϖ [mas yr^{-1}]	12.297±0.015	1
d [pc]	81.27±0.30	1
RV [km s^{-1}]	58.14±0.21	1
U [km s^{-1}]	−29.972±0.056	5[a]
V [km s^{-1}]	−100.23±0.12	5[a]
W [km s^{-1}]	−13.10±−0.19	5[a]
V [mag]	11.48±0.08	2
G_{BP} [mag]	11.599±0.003	1
G [mag]	11.030±0.003	1
G_{RP} [mag]	10.316±0.004	1
J [mag]	9.51±0.03	3
H [mag]	8.94±0.06	3
K [mag]	8.85±0.02	3
$W1$ [mag]	8.76±0.02	4
$W2$ [mag]	8.84±0.02	4
$T_{\rm eff}$ [K]	4687 ± 60	5; spectroscopy
log g [cm s^{-2}]	4.57 ± 0.06	5; spectroscopy
[Fe/H] [dex]	−0.10 ± 0.07	5; spectroscopy
[Mg/H] [dex]	0.02 ± 0.11	5; spectroscopy
[Si/H] [dex]	−0.12 ± 0.09	5; spectroscopy
$V \sin i_\star$ [km s^{-1}]	2.3 ± 0.9	5; spectroscopy
$R_\star$ [R$_\odot$]	0.729 ± 0.007	5; IRFM
$M_\star$ [M$_\odot$]	0.727 ± 0.033	5; isochrones
$t_\star$ [Gyr]	6.3 ± 4.7	5; isochrones
$L_\star$ [L$_\odot$]	0.231 ± 0.013	5; from $R_\star$ and $T_{\rm eff}$
$\rho_\star$ [$\rho_\odot$]	1.88 ± 0.10	5; from $R_\star$ and $M_\star$
$\rho_\star$ [kg m^{-3}]	2645 ± 142	5; from $R_\star$ and $M_\star$

Notes. [1] Gaia Collaboration (2023), [2] E. Høg et al. (2000), [3] M. F. Skrutskie et al. (2006), [4] E. L. Wright et al. (2010), [5] This work
[a]Calculated via the right-handed, heliocentric Galactic spatial velocity formulation of D. R. H. Johnson & D. R. Soderblom (1987) using the proper motions, parallax, and RV from [1].

Averaging of the stellar radius posterior distributions from the two catalogues. This is reported in Table 3.

We then inputted the stellar effective temperature $T_{\rm eff}$, metallicity [Fe/H], and radius $R_\star$ along with their uncertainties in the isochrone placement routine (A. Bonfanti et al. 2015; A. Bonfanti, S. Ortolani & V. Nascimbeni 2016) to derive the stellar mass $M_\star$ and age $t_\star$ from evolutionary models. Following interpolation within pre-computed grids of PARSEC[4] v1.2S (P. Marigo et al. 2017) isochrones and tracks we obtained $M_\star = 0.727 \pm 0.033\,{\rm M}_\odot$ and $t_\star = 6.3 \pm 4.7$ Gyr. All the stellar parameters are listed in Table 3.

3.3 Rotation period

Since ASAS-SN and WASP cover a long baseline of photometric data as shown in Fig. D1, they can be used to identify stellar rotation periods (e.g. T. G. Wilson et al. 2022; D. A. Turner et al. 2025). We hence run a Lomb–Scargle periodogram (N. R. Lomb 1976; J. D. Scargle 1982) on each data set individually, dividing the ASAS-SN data into two sets to cover the V and g-band observations, respectively. We remove peaks due to the cadence of the observations, season length and the moon. The three resulting periodograms for ASAS-SN and WASP respectively are shown in Fig. 3. The two orbital periods of the planets are highlighted in purple and green. Although *TESS* covers a shorter baseline than these two surveys, we run a Lomb–Scargle periodogram on the consecutive sectors 3 and 4 a well as 30 and 31 using the SAP flux and remove the transit signals using WOTAN (M. Hippke et al. 2019). The underlying data as well as the two periodograms are shown in Figs A1 and A2. In all periodograms, we do not find any significant peaks, concluding that TOI-2345 is inactive from these data.

3.4 Kinematic analysis

Gaia DR3 (Gaia Collaboration 2023) reports stellar kinematic properties including the position, parallax, RV, and proper motion of stars. The stellar properties of TOI-2345 measured by *Gaia* are reported in Table 3. D. R. H. Johnson & D. R. Soderblom (1987) derive transformations of coordinates and velocities using the equatorial and galactic coordinates of the star as well as its parallax, RV, and proper motion. Based on the coordinates of the North Galactic Pole and the position angle of the North Celestial Pole, they compute a transformation matrix. Multiplying this matrix with a coordinate matrix constructed for the star and its RV and proper motion the components of the galactic space-velocity can be computed. Performing this computation for TOI-2345, we obtain (U, V, W) = (−29.972±0.056, −100.23±0.12, −13.10±0.19) km s^{-1} in this heliocentric frame. Since this computation is using a right-handed coordinate system, U is positive in the direction of the Galactic Centre, V is positive towards the Galactic rotation, and W is positive towards the North Galactic Pole. Since the galactic space-velocities derived previously are heliocentric, we correct them for the solar motion in the local standards of rest from V. V. Koval', V. A. Marsakov & T. V. Borkova (2009), R. Schönrich, J. Binney & W. Dehnen (2010), B. Coşkunoğlu et al. (2011), V. V. Bobylev and A. T. Bajkova (2014), C. Francis & E. Anderson (2014), H.-J. Tian et al. (2015), and F. Almeida-Fernandes & H. J. Rocha-Pinto (2018).

To compute the galactic kinematic probabilities of the thin disc, thick disc, and halo we follow T. Bensby, S. Feltzing & I. Lundström (2003). They assume that the stellar populations follow Gaussian distributions which are normalized by the characteristic velocity dispersions of each group (σ_U, σ_V, σ_W) and V is corrected using the asymmetric drift. Since the local number densities of each population are different they multiply the probabilities by the observed fraction of each population to obtain the relative likelihood of a star belonging to either population. T. Bensby et al. (2003) report values for the velocity dispersions, stellar fractions and asymmetric drift of each of these populations. However, since their work several other studies have reported their own values which slightly vary. The studies we used in our analysis are T. Bensby et al. (2003, 2014); B. E. Reddy, D. L. Lambert & C. Allende Prieto (2006); D.-C. Chen et al. (2021b). Computing the thick disc probability with all combinations of the local standards of rest and the different velocity dispersions, stellar fractions and asymmetric drifts, we obtained a weighted thick disc probability of 85 per cent. From this kinematic analysis, we conclude that TOI-2345 is in the Milky Way's thick disc. Due to the cool nature of the host star, we are unable to confirm its place in the thick disc chemically.

[4] *PA*dova and T*R*ieste *S*tellar *E*volutionary *C*ode: https://stev.oapd.inaf.it/cgi-bin/cmd

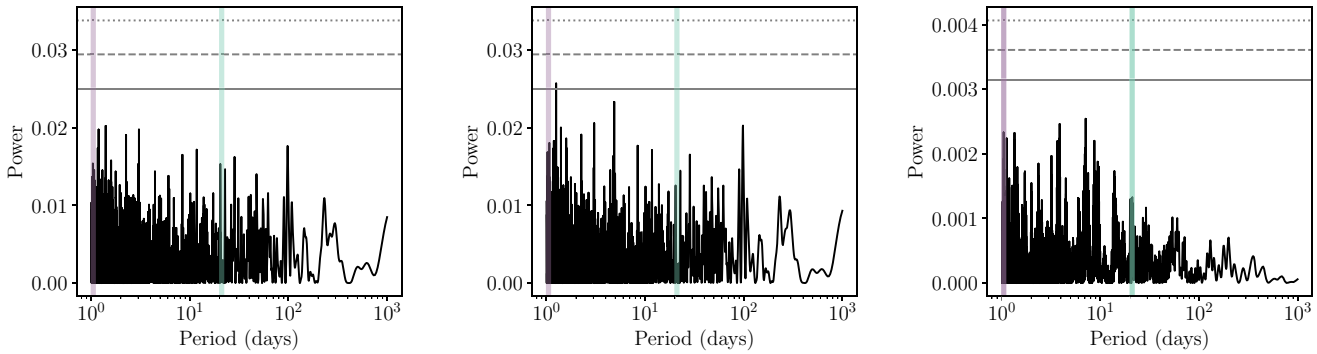

Figure 3. Lomb–Scargle periodogram of TOI-2345 of the ASAS-SN *V* band (left), ASAS-SN *g* band (middle), and WASP (right) data. The orbital periods of the inner and outer planet are highlighted in purple and green, respectively. False Alarm Probabilities of 1 per cent, 0.1 per cent, and 0.01 per cent are shown by the grey continuous, dashed and dotted line, respectively.

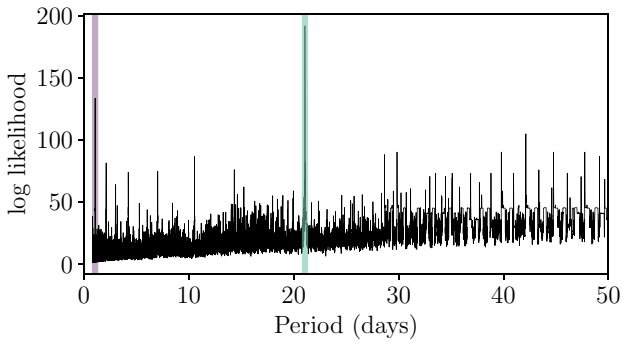

Figure 4. BLS periodogram of the *TESS* light curves of TOI-2345. The two significant peaks are highlighted in purple and green.

4 PLANET FITTING

To understand the planetary properties, we used JULIET (N. Espinoza et al. 2019), a joint fitting tool using BATMAN (L. Kreidberg 2015) for photometric data and RADVEL (B. J. Fulton et al. 2018) to fit the RV data. We make use of JULIET to fit the photometric and RV data individually and jointly. JULIET uses DYNESTY (J. S. Speagle 2020) for nested sampling and computes Bayesian evidences allowing model comparisons. We derive the planetary radii and masses by converting the fitted planet-to-star radius ratios and RV semi-amplitudes fitted in the following and the radius and mass of the star as reported in Section 3.2.

4.1 Photometry

Around this star two planet candidates at periods of 1.05 and 42 d were alerted by the *TESS* team. To verify these, we perform our own search for the periods of the two planets using a Box Least Squares Periodogram (BLS; G. Kovács, S. Zucker & T. Mazeh 2002). This analysis also found a planet at the same period as the *TESS* team, ∼1.05 d, with a log likelihood of logL = 133. The second signal we picked up with logL=192 was at ∼21 d as shown in green in Fig. 4. This signal is half the period that was recorded by the *TESS* vetting team.

A planetary signal of ∼21 d is longer than the continuous *TESS* observations which are downlinked every 13.7 d. Therefore, ∼21 d is a factor of 1.5 times the downlink and sector gaps. Hence, the even transits of the longer period sub-Neptune, TOI-2345 c lie just at the edge of *TESS*'s sector observation gaps and are only partially obtained. We show these two even transits with the best-fitting model in Fig. A3. This caused the *TESS* vetting team to flag the system at twice the period. The *CHEOPS* visit of the outer planet covers the even transit. Based on the transit times alone, we cannot differentiate between the 21 and 42 d period. However, coupling the stellar density with the transit durations from *TESS* and *CHEOPS*, allows us to favour the 21 d period. For this, we run a fit of the *TESS* and *CHEOPS* data in JULIET fitting for the period, P, mid-transit time, t_0, planet-to-star ratio, R_P/R_*, impact parameter, b and stellar density which are summarized in Table 4. Additionally we fit the jitter, the offset relative flux and the limb darkening coefficients parametrized following D. M. Kipping (2013), q_1 and q_2 for each photometric instrument, i.e. *TESS* and *CHEOPS* summarized in Table E1. We included a Gaussian Process (GP) with a Matern-3/2 kernel, implemented in JULIET (S. Ambikasaran et al. 2015; D. Foreman-Mackey et al. 2017), and fitted for the GP amplitude and time-scale as reported in Table E1 to account for any residual systematic noise in the *TESS* photometry. To determine the period of the outer planet we altered its period prior which we set to be uniformly distributed between 10 and 50 d as this includes both possible periods. Since the eccentricity can impact the transit duration, we also let it vary uniformly between 0 and 0.5 as well as the argument of periastron from 0° to 360° for the outer planet in this fit. As shown in Fig. 1, the model picks up the signal of the outer transiting planet at ∼21 d and fits the even transits which are only partially covered by *TESS* observations. This model identifies the 21 d planetary signal which also agrees with our previous BLS search. Hence, we determine a period of 21 d for the outer planet by analysing the *TESS* data carefully to spot transits close to the gaps and accounting for the stellar density in our fit. We use this period for the further analysis.

Using this period and fixed eccentricity, we run joint photometric analyses of the *TESS* and *CHEOPS* data using priors as listed in as listed in Table 4. We run two fits in order to compare the *CHEOPS* aperture photometry obtained from the DRP and the *CHEOPS* PSF photometry obtained by PIPE. In both analyses we apply the same GP as described above to the *TESS* data. The fit using the *TESS* and *CHEOPS* DRP photometry results in radii of 1.48 ± 0.05 and $2.45 \pm 0.05\,R_\oplus$, while the *TESS* and *CHEOPS* PIPE photometry obtain radii of $1.48^{+0.04}_{-0.05}$ and $2.48 \pm 0.06\,R_\oplus$ for the inner and outer planet, respectively. These results are within a 1σ agreement with each other. Since the PIPE photometry (median flux error = 0.00052, RMS=0.00063) has a lower flux uncertainty and RMS than the DRP data (median flux error=0.00056,

Table 4. Fitted and derived planetary parameters. Uniform distributions are noted by $\mathcal{U}$.

		Planet b		Planet c	
Parameter	Unit	Prior	Posterior	Prior	Posterior
T0	(BJD)	$\mathcal{U}(2459116.63, 2459116.83)$	$2459116.7208^{+0.0011}_{-0.0020}$	$\mathcal{U}(2459120.20, 2459120.40)$	$2459120.3007^{+0.0014}_{-0.0013}$
P	(days)	$\mathcal{U}(0.95, 1.15)$	$1.0528573^{+0.0000025}_{-0.0000026}$	$\mathcal{U}(20.96, 21.16)$	$21.064302^{+0.000041}_{-0.000041}$
R_P/R_*		$\mathcal{U}(0, 1)$	$0.01891^{+0.00057}_{-0.00052}$	$\mathcal{U}(0, 1)$	$0.03082^{+0.00049}_{-0.00050}$
b		$\mathcal{U}(0, 1)$	$0.27^{+0.11}_{-0.16}$	$\mathcal{U}(0, 1)$	$0.056^{+0.053}_{-0.037}$
K	($m\,s^{-1}$)	$\mathcal{U}(0, 100)$	$2.71^{+0.66}_{-0.66}$	$\mathcal{U}(0, 100)$	$2.08^{+0.65}_{-0.70}$
			Derived parameters		
a/R_*		–	$5.030^{+0.044}_{-0.049}$	–	$37.07^{+0.32}_{-0.36}$
i	deg	–	$86.9^{+1.3}_{-1.8}$	–	$89.914^{+0.083}_{-0.057}$
R_P	($R_\oplus$)	–	$1.504^{+0.047}_{-0.044}$	–	$2.451^{+0.045}_{-0.046}$
a	(au)	–	$0.01705^{+0.00022}_{-0.00023}$	–	$0.1257^{+0.0016}_{-0.0017}$
M_P	($M_\oplus$)	–	$3.49^{+0.85}_{-0.85}$	–	$7.27^{+2.27}_{-2.45}$
ρ_P	(g/cm^3)	–	$5.64^{+1.48}_{-1.46}$	–	$2.71^{+0.86}_{-0.93}$
T_{eq}	(K)	–	1478 ± 20	–	544 ± 7
S_P	($S_\oplus$)	–	791 ± 43	–	$14.57^{+0.79}_{-0.80}$
TSM		–	43 ± 11	–	33^{+10}_{-11}

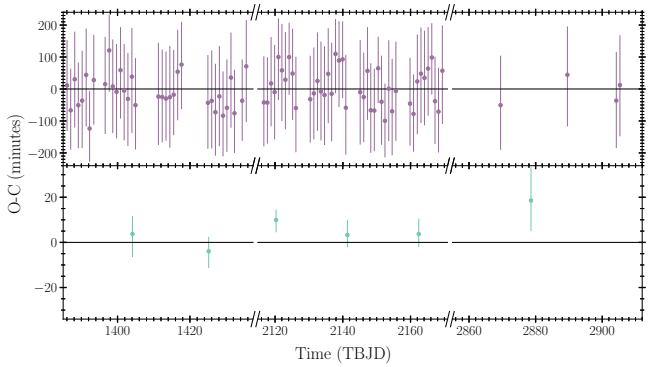

Figure 5. TTV Analysis of TOI-2345. Top: TOI-2345 b in purple. Bottom: TOI-2345 c in green.

RMS=0.00089), we use the *CHEOPS* PIPE data for the further analysis.

Within the *TESS* and *CHEOPS* photometric observations, we checked for transit timing variations that could be caused by potential further planets in the systems. For this we perform a further analysis on the *TESS* and *CHEOPS* data in JULIET. In addition to fitting to the photometric priors used before, we also fit for a perturbation for each transit. This analysis does not identify any significant transit timing variations as shown in Fig. 5. We note that the uncertainties on the transit times of the TOI-2345 b are large. This is due to the very shallow transit, which is challenging for the transit model to identify in individual transits.

4.2 Radial velocity time series assessment

As described in Section 2.3, our S-BART re-extraction resulted in several sets of RVs extracted with different template matching and quality parameters. To determine the optimal RV time series for use in our joint fit, we fitted each of our RV sets in JULIET and kept the period and mid-transit time fixed at the values obtained from the photometry only analysis given their precise determination. In our analysis we allow the semi-amplitudes and HARPS instrumentals (offset and jitter) to vary. Due to the number of RV data points being relatively low, we also kept the eccentricity and argument of periastron fixed at a circular orbit ($e = 0$; $\omega = 90°$). We selected the RV data set that resulted in the lowest jitter in these fits. This was the case for the template matching parameters of an RV step of $0.5\,m\,s^{-1}$ and an RV limit of $200\,m\,s^{-1}$ using the S-BART's classical method. This analysis selected S-BART outputs with quality checks of a minimum order SNR of 1.5, an airmass of 2.2 and RV errors of $5\,m\,s^{-1}$. This set of RV data points has a median error of $2.04\,m\,s^{-1}$ and a RMS of $3.42\,m\,s^{-1}$. We show these re-extracted S-BART RVs in comparison to the DRS RVs in Fig. C1.

Additionally, we searched the activity indicators produced by the HARPS DRS for stellar activity signals using Lomb–Scargle periodograms (N. R. Lomb 1976; J. D. Scargle 1982) for each activity indicator. As in the photometric analysis of stellar activity, we do not find any significant peaks at the 1 per cent false alarm level or lower at typical rotation periods. As no activity indicators peak at the periods of the two planets (highlighted in purple and green in Fig. 6), we conclude that the two signals in the RV data are indeed caused by the two planets and not stellar activity. We also show Lomb–Scargle periodograms of the HARPS DRS and re-extracted S-BART RVs in Fig. 6 showing that there are no significant additional signals that could hint at RV only planets. Given the low number of RVs, there are no significant peaks at the orbital periods of TOI-2345 b and TOI-2345 c. Therefore, we conclude that it is fundamental to jointly fit the photometry and RVs to retrieve the masses for both planets.

4.3 Joint fit

We combine the photometric observations taken by *TESS* and *CHEOPS* with the RV observations taken by HARPS and reprocessed using S-BART in a joint fit. As for our photometric analysis, we apply a GP as described in the photometry to the *TESS* data. Since we did not find a stellar activity signal as shown in Section 3.3, we do not use any GPs for the RV data.

Using JULIET, we fit for the photometric priors as described in Section 4.1 as well as the semi-amplitude, K, for planet b and c, respectively which are summarized in Table 4.

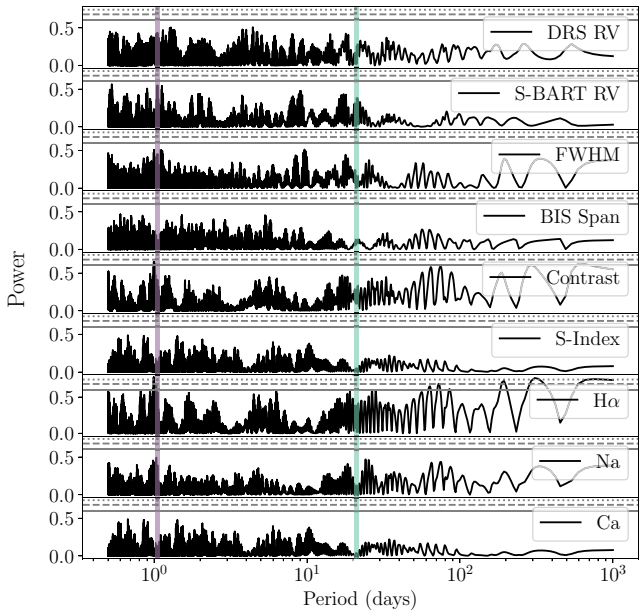

Figure 6. Lomb–Scargle periodograms of the RVs (extracted from the HARPS DRS and S-BART) and activity indicators recorded by the HARPS DRS. The false alarm levels of 1 per cent, 0.1 per cent, and 0.01 per cent are shown by the grey straight, dashed and dotted line, respectively. The orbital periods of the two planets are shown by the purple and green highlights.

Additionally we fit the jitter the offset relative flux and the limb darkening coefficients parametrized following D. M. Kipping (2013), q_1 and q_2 for each photometric instrument, i.e. *TESS* and *CHEOPS*. For the HARPS, we fit the instrumental parameters of the offset and a jitter added in quadrature to the error bars summarized in Table E1.

Due to the limited number of RV observations, we run one fit with the eccentricity and the argument of periastron in our priors fixed resulting in a circular orbit for both planets ($e = 0$, $\omega = 90°$) and another fit where we let them vary uniformly between 0 and 0.5 as well as 0° and 360°, respectively. The eccentric fit allows us to report a 3σ upper limit on the eccentricity of 0.31. Since the circular fit results in a better lnZ (circular: lnZ = 66320, eccentric: lnZ = 66300), we report the results from the circular fit and use these values for the further analysis.

We obtain a radius of $1.504^{+0.047}_{-0.044}\,R_\oplus$ and mass of $3.49 \pm 0.85\,M_\oplus$ for the inner planet, TOI-2345 b, and a radius of $2.451^{+0.045}_{-0.046}\,R_\oplus$ and mass of $7.27^{+2.27}_{-2.45}\,M_\oplus$ for the outer planet, TOI-2345 c. The fitted and derived values are summarized in Table 4. The phase-folded transits and RV curves of this joint fit are shown in Figs 7 and 8, respectively. Given the large upper bounds on the GP hyper-parameters, we conclude that the GP applied to the *TESS* data accounts for residual noise in the photometry.

5 DISCUSSION

5.1 Interior structure modelling

Using the stellar and planetary parameters of the system, we model the interior structure of the two planets using plaNETic (J. A. Egger et al. 2024). plaNETic is an interior structure modelling framework that was first introduced in the analysis of the three planets orbiting TOI-469 (J. A. Egger et al. 2024). As these planets are also in the super-Earth and sub-Neptune regime, this interior structure modelling is tailored well to our planets. plaNETic is using Deep Neural Networks which are trained on mass regimes from 0.5–6 and 6–15 $M_\oplus$ of which both of the planets around TOI-2345 fall. Additionally, each mass range has two different interior structure model databases, one with a water rich and one with a water poor prior represented by the top and bottom row in Figs 9 and 10, respectively.

Within the high and low water prior models, three different priors for the planetary abundances of Fe, Mg, and Si are modelled. These vary from being the same as the stellar abundances as suggested by A. Thiabaud et al. (2015), iron-enriched as suggested by V. Adibekyan et al. (2021) or uniformly sampled with an upper limit of 75 per cent of Fe compared to the other two refractory elements.

As stars and planets are formed from the same material (J. Nielsen et al. 2023) there is a strong connection between the abundances

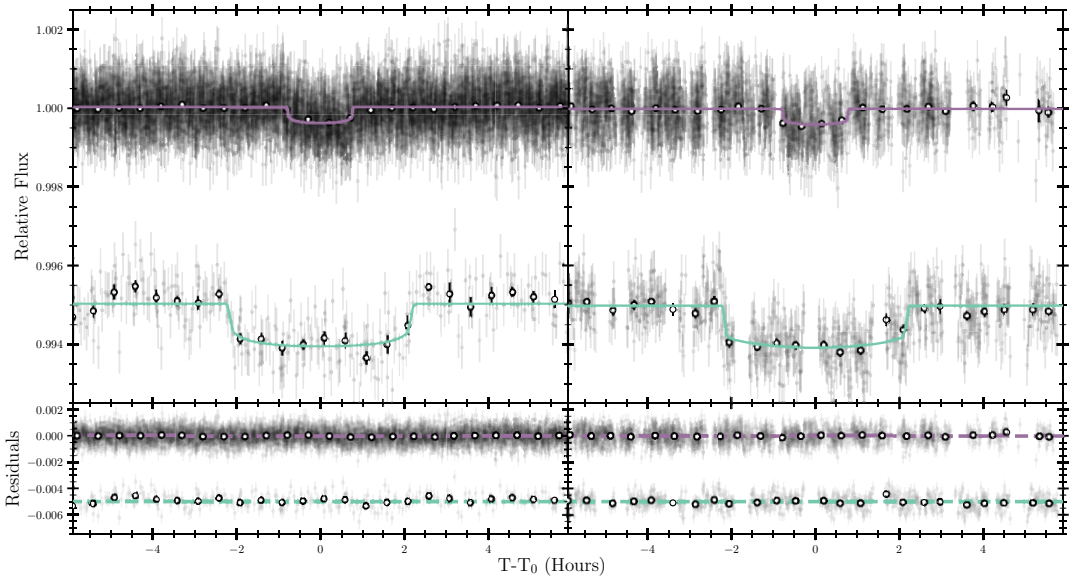

Figure 7. Phase folded transits of TOI-2345 b (purple) and TOI-2345 c (green) with the best-fitting model from the joint fit in JULIET in the top panel. The bottom panel shows the residuals. Left: *TESS* data. Right: *CHEOPS* data.

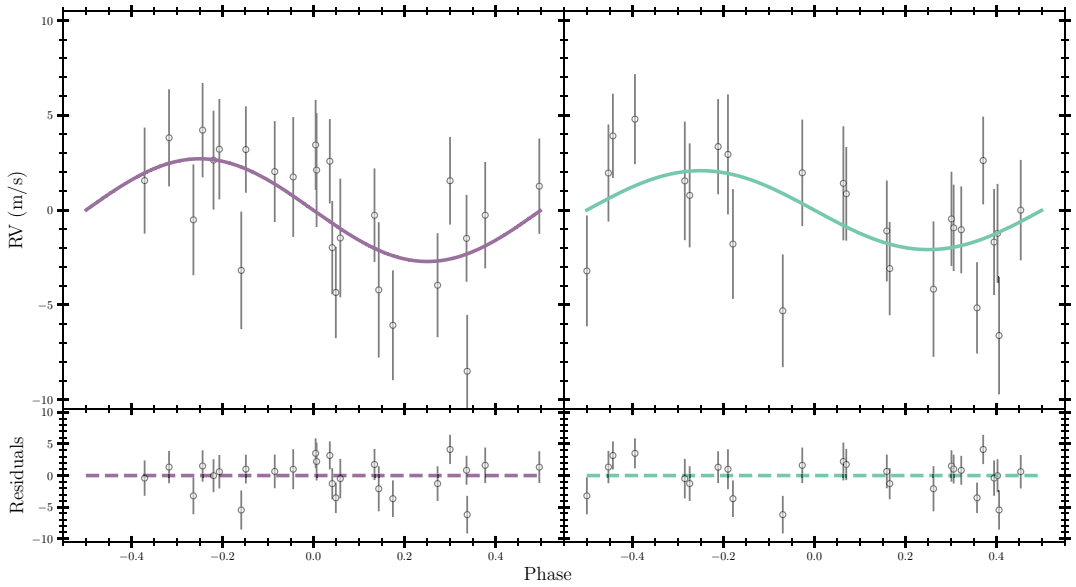

Figure 8. Phase folded RV curves of the HARPS data re-extracted using S-BART of TOI-2345 b in purple on the left and TOI-2345 c in green on the right. The best-fitting model from the joint fit in JULIET in the top panel. The bottom panel shows the residuals.

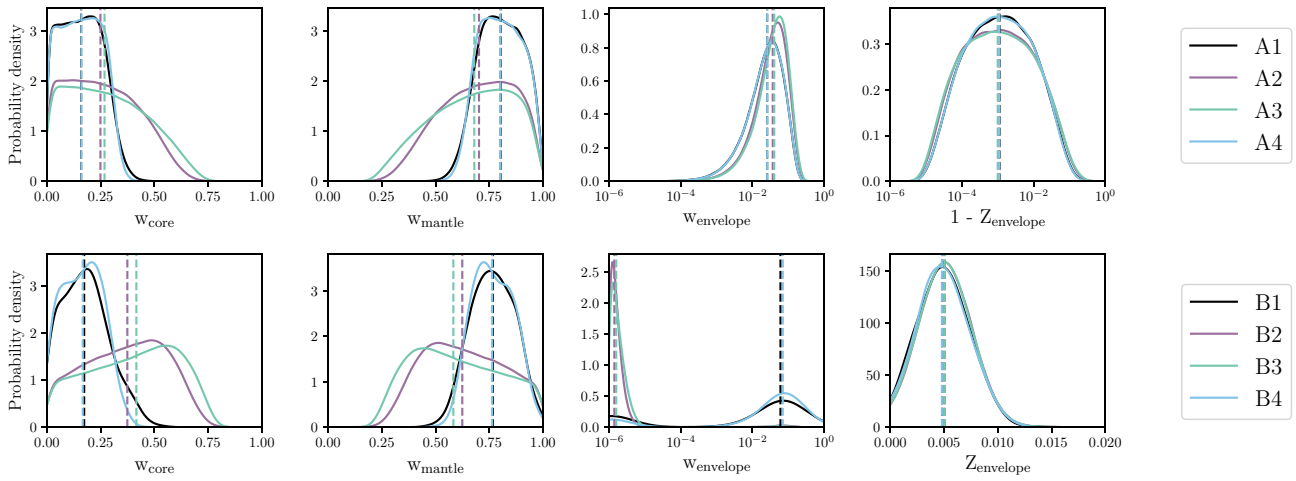

Figure 9. plaNETic posterior distributions for TOI-2345 b. The different abundance priors are shown by the different colours. The median of each posterior is marked by the vertical dashed line. Top: water-rich prior. Bottom: water-poor prior.

of the host star and the planets which can also be seen for the Sun and the Earth (H. S. Wang et al. 2019a). In plaNETic, this is accounted for by the first composition prior. However, this is only the case for refractory elements and not volatiles. Indeed, V. Adibekyan et al. (2021) showed that the connection between stellar and planetary composition may not be one-to-one. H. S. Wang et al. (2019b) developed a tool, ExoInt, to devolatilize stars and obtain the abundances of elements in orbiting planets. Hence we apply ExoInt to our host star in order to obtain the devolatized element abundances that are expected to make up the bulk composition of its orbiting planets. We use the stellar abundances for [Fe/H], [Si/H], and [Mg/H] as recorded in Table 3. ExoInt also requires an abundance of [O/H]. As TOI-2345 is a cool star, it is challenging to determine the oxygen abundance well from the obtained HARPS spectra. So we use the public APOGEE DR17 (D. L. Nidever et al. 2015; S. R. Majewski et al. 2017; Abdurro'uf et al. 2022) catalogue and select stars with the TOI-2345 $T_{\rm eff}$, log g, and [Fe/H] values within the uncertainties. We also remove stars of bad quality flags as recommended by APOGEE. This leaves us with 1265 out of the ∼700000 stars with recorded abundances in APOGEE DR17. Averaging these and their uncertainties, we obtain [O/H] $= -0.09 \pm 0.07$. Using these stellar abundances, we devolatize TOI-2345 using ExoInt. This results in new abundance ratios for the refractory elements of the planets that may reflect the devolatized abundance ratios in the protoplanetary disc better than assuming purely stellar abundances. ExoInt and plaNETic both record the abundances as $10^{[X/Fe]_*}$, where X is Si or Mg. For the stellar abundances in plaNETic, we obtain these to be 1.12 for Si and 1.62 for Mg; using ExoInt they are 1.00 and 1.63 for Si and Mg, respectively. We use these planetary abundances for Mg and Si from ExoInt as an additional prior in plaNETic.

We find the result of this additional model as shown by the pink line in Figs 9 and 10 to be in agreement with the other three priors of plaNETic. Especially, we note that the ExoInt priors (A4 and B4) are similar to the stellar abundances (A1 and B1). However they are

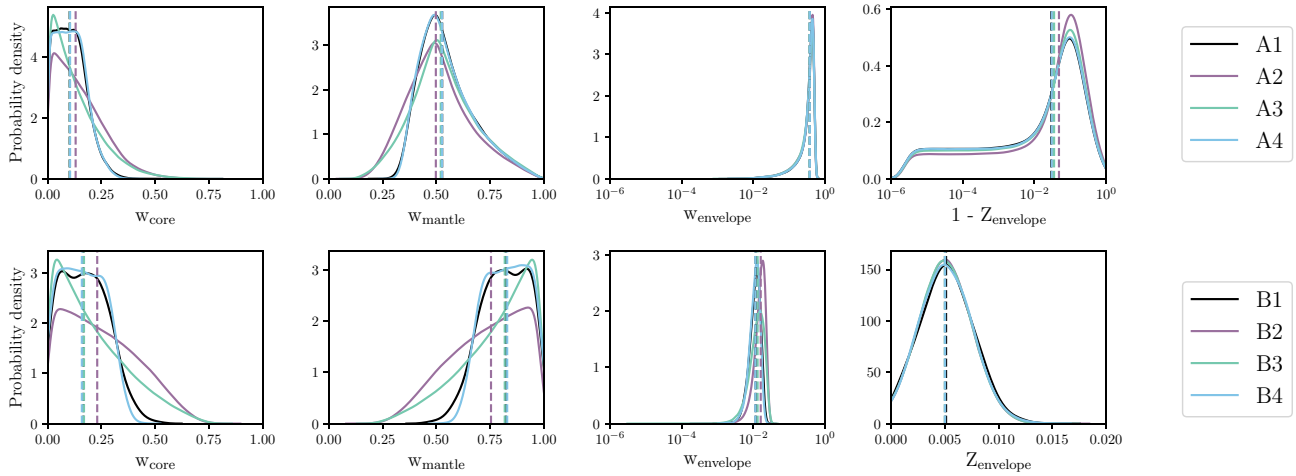

Figure 10. plaNETic posterior distributions for TOI-2345 c. The different abundance priors are shown by the different colours. The median of each posterior is marked by the vertical dashed line. Top: water-rich prior. Bottom: water-poor prior.

Table 5. Core, mantle, water, and atmospheric mass fraction modelled by plaNETic for planet b and c using devolatized stellar abundances from ExoInt (4) and the water-rich (A) and water poor (B) priors.

Planet	Model	CMF	MMF	WMF	AMF
TOI-2345 b	A4	$0.16^{+0.11}_{-0.11}$	$0.80^{+0.11}_{-0.11}$	$0.026^{+0.043}_{-0.019}$	$0.000021^{+0.000185}_{-0.000018}$
TOI-2345 b	B4	$0.167^{+0.099}_{-0.111}$	$0.763^{+0.107}_{-0.094}$	$0.00028^{+0.00034}_{-0.00028}$	$0.070^{+0.039}_{-0.070}$
TOI-2345 c	A4	$0.10^{+0.074}_{-0.071}$	$0.526^{+0.158}_{-0.098}$	$0.367^{+0.094}_{-0.213}$	$0.011^{+0.019}_{-0.011}$
TOI-2345 c	B4	$0.16^{+0.12}_{-0.11}$	$0.83^{+0.11}_{-0.11}$	$0.000053^{+0.000038}_{-0.000029}$	$0.0113^{+0.0034}_{-0.0036}$

slightly higher in the core and lower in the mantle which is due to the devolatizing of ExoInt and hence having slightly higher abundances of refractory (heavier) elements in our priors. As summarized in Table 5, we find from our interior structure analysis that the inner planet has a low core and high mantle mass fraction for the water-poor and water-rich priors. As expected for a highly irradiated super-Earth its atmospheric mass fraction is very low and nominally consistent with 0 for both sets of priors. The outer planet has a similar distribution of core and mantle mass to the inner planet in the water-poor prior. However, the water-rich prior increases the water content of this planet significantly while shrinking the core and mantle mass fractions. Since we do not know the formation path of these planets, we cannot differentiate between the water-rich and water-poor priors.

5.2 Atmospheric evolution modelling

We evaluated the atmospheric evolution of TOI-2345 b and c using the *P*lanetary *A*tmosphere and *S*tellar Ro*T*ation RA*t*e (PASTA; A. Bonfanti et al. 2021) code. The tool works in the Markov chain Monte Carlo (MCMC) framework MC3 developed by P. Cubillos et al. (2017) and at each chain step and for each exoplanet it computes the evolutionary track of the atmospheric mass fraction $f_{atm}(t)$ from the time of dispersal of the proto-planetary disc t_{disc}, assumed to be 5 Myr, up to the present age of the system $t_\star$. To do so, PASTA assumes that: (i) no migration has occurred after t_{disc}, (ii) the atmosphere is H-dominated, and (iii) the atmospheric mass-loss is driven by thermal mechanisms, that is high energy (X-ray + EUV: XUV) flux from the stellar host (photoevaporation; see e.g. H. Lammer et al. 2003; H. Chen & L. A. Rogers 2016) and core-powered mass-loss (e.g. S. Ginzburg, H. E. Schlichting & R. Sari 2018; A. Gupta & H. E. Schlichting 2019).

PASTA is model-dependent and uses the MESA isochrones and stellar tracks (MIST; J. Choi et al. 2016) to trace the evolution of stellar parameters over time, a gyrochronological relation $P_{rot}(t)$ in the form of a broken-power law as presented in A. Bonfanti et al. (2021), a set of empirical relations to convert the stellar rotation period P_{rot} into the emitted XUV-flux at any given epoch (A. Bonfanti et al. 2021, and references therein), a model for computing the atmospheric mass-loss (D. Kubyshkina et al. 2018a, b), and a planetary structure model that links the planetary observables with the expected atmospheric content (C. P. Johnstone et al. 2015b). PASTA requires input parameters both on the stellar side ($M_\star$, $t_\star$, and $P_{rot,\star}$) and on the planetary side (M_p, R_p, and a for each exoplanet in the system). The present-day stellar rotation period $P_{rot,\star}$ has been inferred by inverting the gyrochronological relation from S. A. Barnes & Y.-C. Kim (2010), while all other system parameters are taken from Tables 3 and 4. Once a given MCMC step has been performed, for each planet the code builds its $f_{atm}(t)$, it converts it into the corresponding evolutionary track in radius $R_p(t)$ according to the planetary structure models and checks whether $R_p(t_\star)$ is consistent with the observed R_p. If so, that chain step is accepted and the consequent $f_{atm}(t_{disc}) \equiv f^{start}_{atm}$ value builds up the posterior distribution for the initial atmospheric mass fraction of the planet. As a by-product, we also get the stellar rotation period when the star was young.

Fig. 11 (left panel) compares the posterior distribution of P_{rot} when the star was 150 Myr old (thick blue histogram) with the P_{rot} distribution of stars belonging to 150-Myr-old open clusters and having a mass comparable to $M_\star$ (thin black histogram; taken from C. P. Johnstone et al. 2015a), which suggests that TOI-2345 was likely born as a slow rotator. The other two panels of Fig. 11, instead, show the posterior distribution of f^{start}_{atm} for planet b and c, in comparison with the present-day atmospheric content expected if the atmosphere

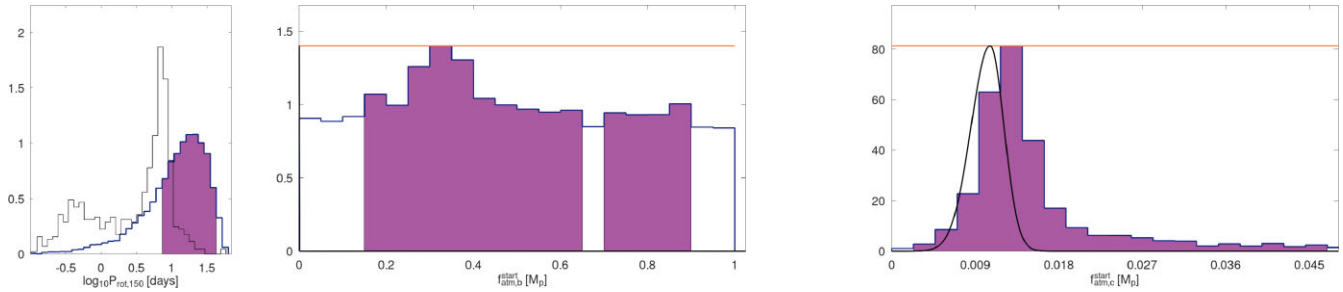

Figure 11. Posterior distributions (thick blue histograms with the underneath area normalized to (1) as outputted by PASTA for the stellar rotation period when the star was 150 Myr old $P_{\rm rot,150}$ (*left panel*) and for the initial atmospheric mass fraction $f_{\rm atm}^{\rm start}$ of TOI-2345 b (*middle panel*) and TOI-2345 c (*right panel*). The purple area represent the 68 per cent highest probability density intervals. The thin black histogram in the left panel depicts the $P_{\rm rot,150}$ distribution of open-cluster stars with masses comparable to that of TOI-2345 as taken from C. P. Johnstone et al. (2015a). The black lines in the *middle* and *right* panels represent the present-day atmospheric content of the planets (which is negligible for TOI-2345 b), while the orange horizontal lines mark that uniform priors were imposed on the $f_{\rm atm}^{\rm start}$ jump parameters. This is in agreement with our interior structure modelling results from plaNETic which also found the inner planet to have a negligible atmosphere, while the atmospheric mass fraction of the outer planet agrees with the present day value found from the atmospheric evolution modelling.

is H-dominated (black line). In the middle panel, the black line is basically compatible with zero (i.e. no atmosphere is expected around the highly irradiated USP) and this condition is reached regardless of $f_{\rm atm}^{\rm start}$. Finally, the right panel shows that the present-day $f_{\rm atm}$ of TOI-2345 c is similar to the inferred $f_{\rm atm}^{\rm start}$, with the planet that has likely lost only a small fraction of its initial atmospheric content.

5.3 Assessment with synthetic planet population

To understand the broader formation and evolution conditions that the TOI-2345 planets have undergone, we placed the system in the context of a synthetic planet population. As host star properties have a strong impact on the underlying physical processes that impact orbiting planets, we retrieved the results of a synthetic population that most closely match the spectral type of TOI-2345 (R. Burn et al. 2021). These simulations of 999 K-dwarf systems each with 50 initial planetary embryos were produced by a detailed formation and evolution framework (A. Emsenhuber et al. 2021). In brief, the embryos undergo formation and growth in a coupled gas and dust disc with the amount of refractory and volatile elements accreted during formation being monitored. This is useful in understanding the interior structures of these synthetic planets. Within the theoretical framework evolution is handled via atmospheric escape, giant impacts, and gas-driven, tidal-forces, and planet–planet scattering migration. Importantly, the evolution of the synthetic planetary systems is also coupled to the evolution of the host star from formation to the end state of the simulation at 5 Gyr.

For our comparative analyses, we selected TOI-2345-like systems following the procedures outlined in J. A. Egger et al. (2024). This was done by taking the TOI-2345 b and c radii, masses, and semimajor axes derived from our joint fit (see Table 4), and choosing synthetic planets within 25 per cent or 3σ (choosing the larger) of the TOI-2345 planets.

To test the tentative stellar-planetary compositional link, we assessed the interior structures of the synthetic planets as a function of stellar metallicity. To do so, we further restrict the TOI-2345 b and c-like planets to those that orbit a star with a similar [Fe/H] to that of TOI-2345. This results in eight TOI-2345 b-like bodies and 16 TOI-2345 c-like planets. For the inner planets, we find core-to-mantle mass ratios of 0.24–0.32 which agrees within 1σ of our value (0.20 ± 0.14) from our A4 interior structure modelling reported in Table 5. Interestingly, the TOI-2345 c-like planets that orbit a compositionally-similar star have more constrained core-to-mantle mass ratios of 0.24–0.25 with a wider range of water and atmospheric mass fractions. Whilst again slightly lower than predicted values, our A4 interior structure modelling core-to-mantle mass ratio for TOI-2345 c (0.19 ± 0.15) also agrees with the synthetic planets.

Given the wide period gap between the two detected TOI-2345 planets, we aimed to search the synthetic systems to understand the rarity of such a configuration when considering the formation and evolution processes include in the framework (A. Emsenhuber et al. 2021). To do this, we selected multiplanet synthetic systems that host at least two bodies that resemble TOI-2345 b and c without the stellar metallicity constraint. Of the 999 systems, only one appears TOI-2345-like via this criteria. However, this synthetic system also includes two additional planets between the TOI-2345 b and c-like bodies with orbital periods of ∼4.0 and 11.5 d. The masses of these bodies (∼7.1 and 11.5 $M_\oplus$) result in RV semi-amplitudes of ∼4.6 and 5.4 $m\,s^{-1}$, respectively. Should such an architecture be present in the TOI-2345 system it would be detectable in our HARPS data as the RMS scatter of the residuals to our HARPS fit is ∼2.6 $m\,s^{-1}$. Given the simulated co-planarity, these additional planets would also be apparent in the *TESS* photometry. However, no such signals exist. While the number of simulated systems we compared to TOI-2345 is relatively small and the theoretical framework may not include all important processes (such as pebble accretion or MHD wind driven discs), it could still provide a good population overview. Therefore, the TOI-2345 system may be considered architecturally rare via this comparison and worthy of future dynamical studies to understand the migration history.

5.4 TOI-2345 in the context of thick disc systems

As computed in Section 3.4, TOI-2345 is kinematically a thick disc star (P(TD) = 85 per cent). In order to compare this system to other kinematic thick disc systems, we download all known exoplanets from the NASA Exoplanet Archive (NASA Exoplanet Archive 2025). As we rely on the stellar kinematic properties recorded by *Gaia* to compute kinematic probabilities, we also filter for targets that have a recorded *Gaia* ID, which leaves us with 5605 planets. To focus on systems hosting small planets that are well characterized, we apply cut-offs of $V < 13$ mag and $R_{\rm P} < 4\,R_\oplus$ determined with a precision better than 10 per cent. To make sure we only include systems with a measured mass we filter for the mass provenance

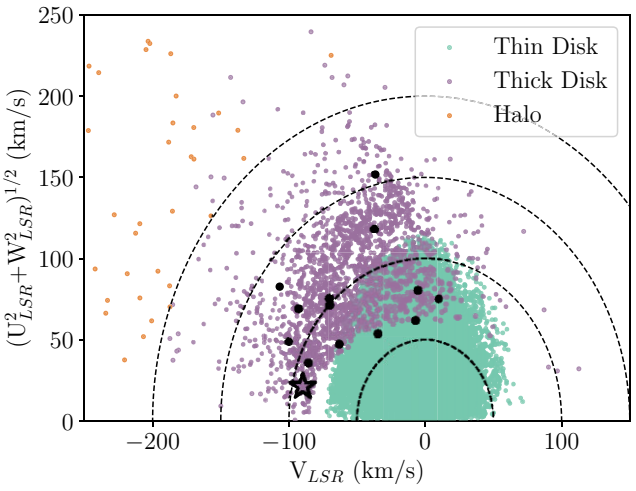

Figure 12. Toomre Diagram of the stellar sample and galactic classifications of D.-C. Chen et al. (2021a). Stars of the thin disc are shown in green, stars of the thick disc in purple and stars of the halo in orange. The well-characterized thick disc systems from Table 6 are shown in black of which the kinematics are computed using the LSR from H.-J. Tian et al. (2015). TOI-2345 is shown by the purple star with the black border and clearly placed in the thick disc.

flag to be 'mass'. We only include systems with $M_P < 30\,M_\oplus$ and measured with a precision better than 30 per cent, similar to our inner planet. This leaves us with 207 planets. In our stellar kinematic analysis, we use the most recent *Gaia* DR3 data, however as the NASA Exoplanet Archive used *Gaia* DR2, we cross-match the *Gaia* DR2 IDs with the *Gaia* DR3 IDs using TOPCAT (M. B. Taylor 2005) and *Gaia*-ARI (Gaia Collaboration 2023). Following the process described in Section 3.4, we compute the kinematic probabilities for each of these systems which are shown in Fig. 13.

Out of the remaining 207 planets, we find that 19 planets are orbiting a host star with a kinematic thick disc probability of above 50 per cent. 12 of these are in multiplanetary system around 6 different host stars. In one of these systems, K2-111 (A. Mortier et al. 2020), the second planet is not transiting and consequently does not have a radius measurement. The second planet orbiting HIP 9618 is only detected with a 3σ upper mass limit (H. P. Osborn et al. 2023). Hence we do not include these two systems in our comparison. The remaining four well-characterized systems are HD 136 352 with a computed weighted thick disc probability of 92 per cent orbited by three small planets (S. Udry et al. 2019; L. Delrez et al. 2021), Kepler-10 with a thick disc probability of 79 per cent that hosts two transiting and one non-transiting small planets (F. Fressin et al. 2011; N. M. Batalha et al. 2011; A. S. Bonomo et al. 2025), TOI-178 that has a thick disc probability of 55 per cent and six small planets out of which three are well characterized to fulfil our comparison criteria (A. Leleu et al. 2021), and HIP 8152 with a computed weighted thick disc probability of 52 per cent orbited by two small planets (J. M. Akana Murphy et al. 2023; A. S. Polanski et al. 2024). As there are only four thick disc systems that contain two or more well-characterized transiting planets below $4\,R_\oplus$, the discovery of the two planets transiting TOI-2345 adds to this limited sample. Among these systems it has the second highest thick disc probability, just below HD 136352, and falls within the range of stellar metallicities.

We demonstrate the location of TOI-2345 in a Toomre diagram in Fig. 12 in which we plot the kinematic properties and galactic classifications of the LAMOST–*Gaia*–*Kepler* sample from D.-C. Chen et al. (2021a). Placing TOI-2345 in context of the other well-characterized systems from Table 6 which are shown in black, we find that TOI-2345 is clearly kinematically a thick disc star.

In order to understand the population of small planets around thick disc stars further and explore trends in their composition, the sample has to be expanded and TOI-2345 contributes to this. For example, the well-characterized interior structures of the TOI-2345 planets can be used to test planet density predictions for thick discs stars in galactic chemical evolution models (J. H. Steffen et al. 2025), and assess planet frequency statistics across stellar kinematic and chemical families (J. Nielsen et al. 2023). J. M. D. Kruijssen, S. N. Longmore & M. Chevance (2020) predicted that planets below the radius valley should be less frequent around low-density phase space stars that are predominantly found in the Galactic thick disc (A. J. Mustill, M. Lambrechts & M. B. Davies 2022). The super-Earth and sub-Neptune orbiting TOI-2345 span the radius valley as shown in Fig. 13 and so provide evidence to refute this prediction. This is also found for HD 136352, Kepler-10, and TOI-178. However, also this is still a very restricted sample and so importantly TOI-2345 adds to this.

Additionally, TOI-2345 b is on a 1 d orbit and hence also increases the sample of USPs around thick disc stars. In combination with the wider orbital spacing of planets b and c, the TOI-2345 system is in agreement with the broader stellar kinematic-planet architecture trends seen in a *Kepler*-based sample of USPs (J. N. Winn et al. 2018; P.-W. Tu et al. 2025). Following A. Castro-González et al. (2025), USPs could have formed through high-eccentricity migration (C. Petrovich et al. 2019), low-eccentricity migration (B. Pu & D. Lai 2019) or obliquity-driven migration (S. C. Millholland & C. Spalding 2020). As we do not find a high eccentricity for TOI-2345 b which could hint at high-eccentricity migration, nor planetary neighbours in close-in orbits in <10 d, which are expected in a obliquity-driven migration scenario, the most likely formation of TOI-2345 is the low-eccentricity scenario.

6 CONCLUSIONS

We present the discovery of a super-Earth and sub-Neptune orbiting the thick disc star TOI-2345. We detected these two planets using photometry from *TESS* and *CHEOPS*, and RV observations from HARPS. We characterized the star to be slightly metal-poor and kinematically determined that TOI-2345 is a member of the Milky Way's thick disc. The photometric and spectroscopic observations allowed us to derive a radius of $1.504^{+0.047}_{-0.044}\,R_\oplus$ and $2.451^{+0.045}_{-0.046}\,R_\oplus$ and mass of $3.49^{+0.85}_{-0.85}\,M_\oplus$ and $7.27^{+2.27}_{-2.45}\,M_\oplus$ for the inner and outer planet orbiting the star at periods of 1.05 and $\sim$21 d, respectively. The accurate determination of the radii and masses of these planets enabled us to model the interior structure using plaNETic. To account for the connection in refractory elements between host stars and planets, we devolatize the host star with ExoInt and use the obtained abundances as priors in our interior modelling for the first time. This results in predicted interior structures which are in agreement to the interior structures obtained when using the stellar abundances as a prior. We obtained the interior structure of the inner rocky planet to have a large mantle, small core and nearly no atmosphere, while the outer planet also has a small core and large mantle but is gas-rich and has an atmospheric mass fraction of approximately 1 per cent. Additionally, performing atmospheric escape modelling we find that the Ultra-Short-Period inner super-Earth has lost its atmosphere, while the outer sub-Neptune has likely only lost a small fraction of its initial atmosphere. Finally, we place the TOI-2345 system in the context of thick disc stars. The characterization of TOI-2345, which contains a USP super-Earth below the radius valley, demonstrates that such small planets around thick disc stars are more common

Table 6. Well-characterized planet below 4 $R_\oplus$ orbiting kinematically thick disc stars. References: [1] A. Mortier et al. (2020), [2] A. S. Bonomo et al. (2023), [3] A. Shporer et al. (2020), [4] R. Luque & E. Pallé (2022), [5] J. M. Akana Murphy et al. (2023), [6] A. S. Polanski et al. (2024), [7] M. S. Peterson et al. (2018), [8] A. W. Mayo et al. (2018), [9] E. Thygesen et al. (2023), [10] S. Udry et al. (2019), [11] L. Delrez et al. (2021), [12] M. Montalto et al. (2024), [13] N. Heidari et al. (2025), [14] N. M. Batalha et al. (2011), [15] A. S. Bonomo et al. (2025), [16] F. Fressin et al. (2011), [17] J. A. Burt et al. (2021), [18] F. Murgas et al. (2022), [19] A. Leleu et al. (2021), [20] H. P. Osborn et al. (2023).

Planet	R_P ($R_\oplus$)	M_P ($M_\oplus$)	ρ_P (g/cm^3)	T_{eq} K	P(TD)	[Fe/H]	#planets	Reference
K2-111 b	$1.820^{+0.11}_{-0.090}$	$5.58^{+0.74}_{-0.73}$	$5.0^{+1.1}_{-1.0}$	1309 ± 19	0.991	-0.46 ± 0.05	2	[1,2]
GJ 1252 b	1.193 ± 0.074	1.32 ± 0.28	$4.2^{+1.3}_{-1.1}$	1089 ± 69	0.987	$+0.1 \pm 0.1$	1	[3,4]
TOI-669 b	$2.59^{+0.13}_{-0.11}$	10.0 ± 1.4	$3.17^{+0.73}_{-0.95}$	1125 ± 19	0.965	-0.06 ± 0.09	1	[5,6]
Wolf 503 b	2.043 ± 0.069	$6.27^{+0.85}_{-0.84}$	$4.03^{+0.72}_{-0.64}$	789 ± 16	0.965	-0.47 ± 0.08	1	[7,2]
K2-180 b	$2.466^{+0.110}_{-0.096}$	$11.4^{+2.4}_{-2.2}$	$4.16^{+1.10}_{-0.92}$	$797.5^{+8.4}_{-8.5}$	0.953	-0.65 ± 0.10	1	[8,9]
HD 136352 b	1.664 ± 0.043	4.72 ± 0.42	$5.62^{+0.72}_{-0.66}$	905 ± 14	0.926	-0.24 ± 0.05	3	[10,11]
HD 136352 c	$2.916^{+0.075}_{-0.073}$	$11.24^{+0.65}_{-0.63}$	$2.50^{+0.25}_{-0.23}$	677 ± 11	0.926	-0.24 ± 0.05	3	[10,11]
HD 136352 d	$2.562^{+0.088}_{-0.079}$	$8.82^{+0.93}_{-0.92}$	$2.88^{+0.43}_{-0.40}$	431 ± 7	0.926	-0.24 ± 0.05	3	[10,11]
TOI-5076 b	$3.489^{+0.100}_{-0.094}$	16.1 ± 2.5	$2.08^{+0.35}_{-0.34}$	550 ± 14	0.921	$+0.20 \pm 0.08$	1	[12,13]
TOI-2345 b	$1.504^{+0.047}_{-0.044}$	3.49 ± 0.85	$5.64^{+1.48}_{-1.46}$	1478 ± 20	0.850	-0.10 ± 0.07	2	This work
TOI-2345 c	$2.451^{+0.045}_{-0.046}$	$7.27^{+2.27}_{-2.45}$	$2.71^{+0.86}_{-0.93}$	544 ± 7	0.850	-0.10 ± 0.07	2	This work
Kepler-10 b	$1.47^{+0.03}_{-0.02}$	3.24 ± 0.32	$5.54^{+0.66}_{-0.62}$	2188 ± 16	0.789	-0.15 ± 0.04	3	[14,15]
Kepler-10 c	2.355 ± 0.022	11.29 ± 1.24	4.75 ± 0.53	579 ± 4	0.789	-0.15 ± 0.04	3	[16,15]
TOI-1231 b	$3.65^{+0.16}_{-0.15}$	15.4 ± 3.3	$1.74^{+0.47}_{-0.42}$	$329.6^{+3.8}_{-3.7}$	0.785	$+0.05 \pm 0.08$	1	[17]
HD 20329 b	1.72 ± 0.07	7.42 ± 1.09	8.06 ± 1.53	2141 ± 27	0.621	-0.07 ± 0.06	1	[18]
TOI-178 b	$1.152^{+0.073}_{-0.070}$	$1.50^{+0.39}_{-0.44}$	$5.4^{+1.9}_{-1.7}$	1040^{+22}_{-21}	0.545	-0.23 ± 0.05	6	[19]
TOI-178 c	$1.669^{+0.114}_{-0.099}$	$4.77^{+0.55}_{-0.68}$	$5.62^{+1.50}_{-1.30}$	873 ± 18	0.545	-0.23 ± 0.05	6	[19]
TOI-178 f	$2.287^{+0.108}_{-0.110}$	$7.72^{+1.67}_{-1.52}$	$3.60^{+1.20}_{-0.83}$	521 ± 11	0.545	-0.23 ± 0.05	6	[19]
HIP 9618 b	3.75 ± 0.13	8.40 ± 2.00	0.90 ± 0.20	685 ± 17	0.528	-0.10 ± 0.09	2	[20,5]
HIP 8152 b	$2.54^{+0.16}_{-0.14}$	8.90 ± 1.70	$2.97^{+0.81}_{-1.08}$	795^{+14}_{-13}	0.525	-0.09 ± 0.09	2	[5,6]
HIP 8152 c	$2.52^{+0.15}_{-0.14}$	$10.7^{+2.1}_{-2.2}$	$3.63^{+1.02}_{-1.38}$	651 ± 11	0.525	-0.09 ± 0.09	2	[5,6]

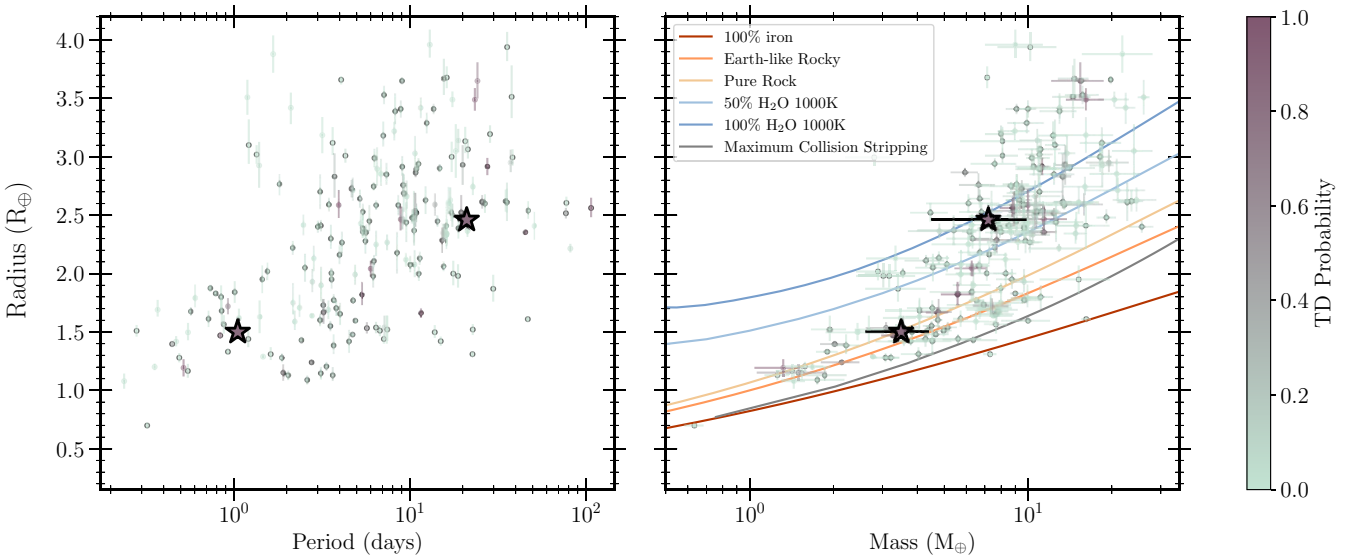

Figure 13. Comparison of the two planets orbiting TOI-2345 to other well characterized planets below 4 $R_\oplus$ colour-coded by the respective weighted kinematic thick disc probability of the host star. TOI-2345 is shown by the stars in purple with the black border, where the colour is representing its high thick disc probability. Multiplanetary systems are highlighted by circles. Left: Radius-Period diagram. Right: Radius-mass diagram. We show compositional lines for 100 per cent iron, Earth-like rocky, pure rock, 100 per cent water at 1000 K and 50 per cent water at 1000 K at the respected colour-coded lines following L. Zeng et al. (2019). Additionally, we show the maximum collision stripping following R. A. Marcus et al. (2010) by the grey line.

than previously thought. Moreover, the orbital period of the planets infer that the USP underwent low-eccentricity migration. Since only a limited sample of small planets around thick disc stars has been well characterized to date, TOI-2345 adds on to this sample which will enable demographic studies of planets in this stellar population in the future.

ACKNOWLEDGEMENTS

We thank the anonymous reviewer for their feedback. *CHEOPS* is an ESA mission in partnership with Switzerland with important contributions to the payload and the ground segment from Austria, Belgium, France, Germany, Hungary, Italy, Portugal, Spain, Sweden, and the United Kingdom. The *CHEOPS* Consortium would like to gratefully acknowledge the support received by all the agencies, offices, universities, and industries involved. Their flexibility and willingness to explore new approaches were essential to the success of this mission. *CHEOPS* data analysed in this article will be made available in the *CHEOPS* mission archive (https://cheops.unige.ch/archive_browser/). Funding for the *TESS* mission is provided by NASA's Science Mission Directorate. We acknowledge the use of public *TESS* data from pipelines at the *TESS* Science Office and at the *TESS* Science Processing Operations Center. This research has made use of the Exoplanet Follow-up Observation Programme website, which is operated by the California Institute of Technology, under contract with the National Aeronautics and Space Administration under the Exoplanet Exploration Programme. YNEE acknowledges support from a Science and Technology Facilities Council (STFC) studentship, grant no. ST/Y509693/1. TWi acknowledges support from the UKSA and the University of Warwick. SGS acknowledge support from FCT through FCT contract nr. CEECIND/00826/2018 and POPH/FSE (EC). The Portuguese team thanks the Portuguese Space Agency for the provision of financial support in the framework of the PRODEX Programme of the European Space Agency (ESA) under contract number 4000142255. ML acknowledges support of the Swiss National Science Foundation under grant no. PCEFP2_194576. AS acknowledges support from the Swiss Space Office through the ESA PRODEX programme. This work has been carried out within the framework of the NCCR PlanetS supported by the Swiss National Science Foundation under grants 51NF40_182901 and 51NF40_205606. AJM acknowledges the support of the Swedish National Space Agency (grant 2023–00146). HV acknowledges funding from the Institut Universitaire de France (IUF) that made this work possible. YAl acknowledges support from the Swiss National Science Foundation (SNSF) under grant 200020_192038. DB, EP, EV, IR, and RA acknowledge financial support from the Agencia Estatal de Investigación of the Ministerio de Ciencia e Innovación MCIN/AEI/10.13039/501100011033 and the ERDF 'A way of making Europe' through projects PID2021-125627OB-C31, PID2021-125627OB-C32, PID2021-127289NB-I00, PID2023-150468NB-I00, and PID2023-149439NB-C41,. from the Centre of Excellence 'Severo Ochoa' award to the Instituto de Astrofísica de Canarias (CEX2019-000920-S), the Centre of Excellence 'María de Maeztu' award to the Institut de Ciències de l'Espai (CEX2020-001058-M), and from the Generalitat de Catalunya/CERCA programme. SCCB acknowledges the support from Fundação para a Ciência e Tecnologia (FCT) in the form of work contract through the Scientific Employment Incentive programme with reference 2023.06687.CEECIND and DOI 10.54499/2023.06687.CEECIND/CP2839/CT0002. LBo, GBr, VNa, IPa, GPi, RRa, GSc, VSi, and TZi acknowledge support from *CHEOPS* ASI-INAF agreement no. 2019-29-HH.0. ABr was supported by the SNSA. CB acknowledges support from the Swiss Space Office through the ESA PRODEX programme. ACC acknowledges support from STFC consolidated grant no. ST/V000861/1 and UKRI/ERC Synergy grant EP/Z000181/1 (REVEAL). ACMC acknowledges support from the FCT, Portugal, through the CFisUC projects UIDB/04564/2020 and UIDP/04564/2020, with DOI identifiers 10.54499/UIDB/04564/2020 and 10.54499/UIDP/04564/2020, respectively. AC, AD, BE, KG, and JK acknowledge their role as ESA-appointed *CHEOPS* Science Team Members. PEC is funded by the Austrian Science Fund (FWF) Erwin Schroedinger Fellowship, programme J4595-N. This project was supported by the CNES. A.De. This work was supported by FCT – Fundação para a Ciência e a Tecnologia through national funds and by FEDER through COMPETE2020 through the research grants UIDB/04434/2020, UIDP/04434/2020, 2022.06962.PTDC. ODSD is supported in the form of work contract (DL 57/2016/CP1364/CT0004) funded by national funds through FCT. BOD acknowledges support from the Swiss State Secretariat for Education, Research and Innovation (SERI) under contract number MB22.00046. AC, AD, BE, KG, and JK acknowledge their role as ESA-appointed *CHEOPS* Science Team Members. This project has received funding from the Swiss National Science Foundation for project 200021_200726. It has also been carried out within the framework of the National Centre of Competence in Research PlanetS supported by the Swiss National Science Foundation under grant 51NF40_205606. The authors acknowledge the financial support of the SNSF. MF and CMP gratefully acknowledge the support of the Swedish National Space Agency (DNR 65/19, 174/18). DG gratefully acknowledges financial support from the CRT foundation under grant no. 2018.2323 'Gaseousor rocky? Unveiling the nature of small worlds'. MG is an F.R.S.-FNRS Senior Research Associate. MNG is the ESA *CHEOPS* Project Scientist and Mission Representative. BMM is the ESA *CHEOPS* Project Scientist. KGI was the ESA *CHEOPS* Project Scientist until the end of December 2022 and Mission Representative until the end of January 2023. All of them are/were responsible for the Guest Observers (GO) Programme. None of them relay/relayed proprietary information between the GO and Guaranteed Time Observation (GTO) Programmes, nor do/did they decide on the definition and target selection of the GTO Programme. CHe acknowledges financial support from the Österreichische Akademie 1158 der Wissenschaften and from the European Union H2020-MSCA-ITN-2019 1159 under grant agreement no. 860470 (CHAMELEON). Calculations were performed using supercomputer resources provided by the Vienna Scientific Cluster (VSC). AC, AD, BE, KG, and JK acknowledge their role as ESA-appointed *CHEOPS* Science Team Members. The authors acknowledge support from the Swiss NCCR PlanetS and the Swiss National Science Foundation. This work has been carried out within the framework of the NCCR PlanetS supported by the Swiss National Science Foundation under grants 51NF40182901 and 51NF40205606. J.K. acknowledges support from the Swiss National Science Foundation under grant no. TMSGI2_211697. KWFL was supported by Deutsche Forschungsgemeinschaft grants RA714/14-1 within the DFG Schwerpunkt SPP 1992, Exploring the Diversity of Extrasolar Planets. This work was granted access to the HPC resources of MesoPSL financed by the Region Ile de France and the project Equip@Meso (reference ANR-10-EQPX-29-01) of the programme Investissements d'Avenir supervised by the Agence Nationale pour la Recherche. This work has been carried out within the framework of the NCCR PlanetS supported by the Swiss National Science Foundation under grants 51NF40_182901 and 51NF40_205606. AL acknowledges support of the Swiss National Science Foundation under grant no. TMSGI2_211697. PM

acknowledges support from STFC research grant no. ST/R000638/1. This work was also partially supported by a grant from the Simons Foundation (PI Queloz, grant no. 327127). NCS is co-funded by the European Union (ERC, FIERCE, 101052347). Views and opinions expressed are however those of the author(s) only and do not necessarily reflect those of the European Union or the European Research Council. Neither the European Union nor the granting authority can be held responsible for them. This work was supported by FCT – Fundação para a Ciência e a Tecnologia through national funds by these grants: UIDB/04434/2020 DOI: 10.54499/UIDB/04434/2020, UIDP/04434/2020 DOI: 10.54499/UIDP/04434/2020. GyMSz acknowledges the support of the Hungarian National Research, Development and Innovation Office (NKFIH) grant K-125015, a a PRODEX Experiment Agreement No. 4000137122, the Lendület LP2018-7/2021 grant of the Hungarian Academy of Science and the support of the city of Szombathely. VVG is an FRS-FNRS Research Associate. JV acknowledges support from the Swiss National Science Foundation (SNSF) under grant PZ00P2_208945. NAW acknowledges UKSA grant ST/R004838/1.

DATA AVAILABILITY

The data underlying this article will be made available in the *CHEOPS* mission archive https://cheops.unige.ch/archive_browser/. This paper includes data collected by the *TESS* mission, which is publicly available from the Mikulski Archive for Space Telescopes (MAST) at the Space Telescope Science Institute (STScI) https://mast.stsci.edu.

REFERENCES

Abdurro'uf et al., 2022, ApJS, 259, 35
Adams E. R. et al., 2021, PSJ, 2, 152
Adibekyan V. et al., 2021, Science, 374, 330
Adibekyan V. et al., 2024, A&A, 692, A67
Akana Murphy J. M. et al., 2023, AJ, 166, 153
Almeida-Fernandes F., Rocha-Pinto H. J., 2018, MNRAS, 476, 184
Ambikasaran S., Foreman-Mackey D., Greengard L., Hogg D. W., O'Neil M., 2015, IEEE Trans. Pattern Anal. Mach. Intell., 38, 252
Armitage P. J., 2020, Astrophysics of Planet Formation, 2nd edn. Cambridge Univ. Press, Cambridge
Barnes S. A., Kim Y.-C., 2010, ApJ, 721, 675
Batalha N. M. et al., 2011, ApJ, 729, 27
Batalha N. M. et al., 2013, ApJS, 204, 24
Baumeister P., Tosi N., 2023, A&A, 676, A106
Bensby T., Feltzing S., Lundström I., 2003, A&A, 410, 527
Bensby T., Feltzing S., Oey M. S., 2014, A&A, 562, A71
Benz W. et al., 2021, Exp. Astron., 51, 109
Blackwell D. E., Shallis M. J., 1977, MNRAS, 180, 177
Bobylev V. V. and Bajkova A. T., 2014, MNRAS, 441, 142
Bonfanti A., Ortolani S., Piotto G., Nascimbeni V., 2015, A&A, 575, A18
Bonfanti A., Ortolani S., Nascimbeni V., 2016, A&A, 585, A5
Bonfanti A., Fossati L., Kubyshkina D., Cubillos P. E., 2021, A&A, 656, A157
Bonomo A. S. et al., 2023, A&A, 677, A33
Bonomo A. S. et al., 2025, A&A, 696, A233
Borucki W. J. et al., 2010, Science, 327, 977
Brandeker A., Patel J. A., Morris B. M., 2024, Astrophysics Source Code Library, record ascl:2404.002
Burke C. J. et al., 2020, Astrophysics Source Code Library, record ascl:2003.001
Burn R., Schlecker M., Mordasini C., Emsenhuber A., Alibert Y., Henning T., Klahr H., Benz W., 2021, A&A, 656, A72
Burn R., Mordasini C., Mishra L., Haldemann J., Venturini J., Emsenhuber A., Henning T., 2024, Nat. Astron., 8, 463
Burt J. A. et al., 2021, AJ, 162, 87
Caldwell D. A. et al., 2020, Res. Notes Am. Astron. Soc., 4, 201
Castelli F., Kurucz R. L., 2003, in Piskunov N., Weiss W. W., Gray D. F., eds, Proc. IAU Symp. 210, Modelling of Stellar Atmospheres. Astron. Soc. Pac., San Francisco, p. A20
Castro-González A. et al., 2025, A&A, 699, A344
Chen D.-C. et al., 2021a, AJ, 162, 100
Chen D.-C. et al., 2021b, ApJ, 909, 115
Chen H., Rogers L. A., 2016, ApJ, 831, 180
Choi J., Dotter A., Conroy C., Cantiello M., Paxton B., Johnson B. D., 2016, ApJ, 823, 102
Christiansen J. L. et al., 2012, PASP, 124, 1279
Coşkunoğlu B. et al., 2011, MNRAS, 412, 1237
Coughlin J. L. et al., 2016, ApJS, 224, 12
Cubillos P., Harrington J., Loredo T. J., Lust N. B., Blecic J., Stemm M., 2017, AJ, 153, 3
Dai F., Masuda K., Winn J. N., 2018, ApJ, 864, L38
Dai F., Masuda K., Winn J. N., Zeng L., 2019, ApJ, 883, 79
Delrez L. et al., 2021, Nat. Astron., 5, 775
Egger J. A. et al., 2024, A&A, 688, A223
Emsenhuber A., Mordasini C., Burn R., Alibert Y., Benz W., Asphaug E., 2021, A&A, 656, A69
Eschen Y. N. E., Kunimoto M., 2024, MNRAS, 531, 5053
Eschen Y. N. E., Bayliss D., Wilson T. G., Kunimoto M., Pelisoli I., Rodel T., 2024, MNRAS, 535, 1778
Espinoza N., Kossakowski D., Brahm R., 2019, MNRAS, 490, 2262
Feliz D. L., Plavchan P., Bianco S. N., Jimenez M., Collins K. I., Villarreal Alvarado B., Stassun K. G., 2021, AJ, 161, 247
Foreman-Mackey D., Agol E., Angus R., Ambikasaran S., 2017, AJ, 154, 220
Francis C., Anderson E., 2014, Celest. Mech. Dyn. Astron., 118, 399
Fressin F. et al., 2011, ApJS, 197, 5
Fuhrmann K., 1998, A&A, 338, 161
Fulton B. J. et al., 2017, AJ, 154, 109
Fulton B. J., Petigura E. A., Blunt S., Sinukoff E., 2018, PASP, 130, 044504
Gaia Collaboration, 2023, A&A, 674, A1
Ginzburg S., Schlichting H. E., Sari R., 2018, MNRAS, 476, 759
Gondoin P., 2024, A&A, 690, A369
González Hernández J. I. et al., 2024, A&A, 690, A79
Goyal A. V., Wang S., 2025, AJ, 169, 191
Guerrero N. M. et al., 2021, ApJS, 254, 39
Gupta A., Schlichting H. E., 2019, MNRAS, 487, 24
Hayden M. R. et al., 2015, ApJ, 808, 132
Heidari N. et al., 2025, A&A, 694, A36
Hippke M., David T. J., Mulders G. D., Heller R., 2019, AJ, 158, 143
Ho C. S. K., Van Eylen V., 2023, MNRAS, 519, 4056
Høg E. et al., 2000, A&A, 355, L27
Howard A. W. et al., 2012, ApJS, 201, 15
Howell S. B. et al., 2014, PASP, 126, 398
Hoyer S., Guterman P., Demangeon O., Sousa S. G., Deleuil M., Meunier J. C., Benz W., 2020, A&A, 635, A24
Huang C., Rice D. R., Steffen J. H., 2022, MNRAS, 513, 5256
Jenkins J. M. et al., 2010, ApJ, 713, L87
Jenkins J. M. et al., 2016, in Chiozzi G., Guzman J. C., eds, Proc. SPIE Conf. Ser. Vol. 9913, Software and Cyberinfrastructure for Astronomy IV. SPIE, Bellingham, p. 99133E
Johnson D. R. H., Soderblom D. R., 1987, AJ, 93, 864
Johnstone C. P., Güdel M., Brott I., Lüftinger T., 2015a, A&A, 577, A28
Johnstone C. P. et al., 2015b, ApJ, 815, L12
Jurgenson C., Fischer D., McCracken T., Sawyer D., Szymkowiak A., Davis A., Muller G., Santoro F., 2016, in Evans C. J., Simard L., Takami H., eds, Proc. SPIE Conf. Ser. Vol. 9908, Ground-based and Airborne Instrumentation for Astronomy VI. SPIE, Bellingham, p. 99086T
Kipping D. M., 2013, MNRAS, 435, 2152
Kochanek C. S. et al., 2017, PASP, 129, 104502
Kovács G., Zucker S., Mazeh T., 2002, A&A, 391, 369
Koval' V. V., Marsakov V. A., Borkova T. V., 2009, Astron. Rep., 53, 1117
Kreidberg L., 2015, Astrophysics Source Code Library, record ascl:1510.002

Kruijssen J. M. D., Longmore S. N., Chevance M., 2020, ApJ, 905, L18
Kubyshkina D., Fossati L., 2022, A&A, 668, A178
Kubyshkina D. et al., 2018a, A&A, 619, A151
Kubyshkina D. et al., 2018b, ApJ, 866, L18
Kunimoto M. et al., 2025, AJ, 170, 21
Kurucz R. L., 1993, Kurucz CD-ROM. Smithsonian Astrophysical Observatory, Cambridge
Kurucz R. L., 2013, Astrophysics Source Code Library, record ascl: 1303.024
Lammer H., Selsis F., Ribas I., Guinan E. F., Bauer S. J., Weiss W. W., 2003, ApJ, 598, L121
Leleu A. et al., 2021, A&A, 649, A26
Lindegren L. et al., 2021, A&A, 649, A4
Lomb N. R., 1976, Ap&SS, 39, 447
Lovis C., Pepe F., 2007, A&A, 468, 1115
Luque R., Pallé E., 2022, Science, 377, 1211
Majewski S. R. et al., 2017, AJ, 154, 94
Marcus R. A., Sasselov D., Hernquist L., Stewart S. T., 2010, ApJ, 712, L73
Marigo P. et al., 2017, ApJ, 835, 77
Maxted P. F. L. et al., 2023, Astrophysics Source Code Library, record ascl:2312.034
Mayo A. W. et al., 2018, AJ, 155, 136
Mayor M., Queloz D., 1995, Nature, 378, 355
Mayor M. et al., 2003, The Messenger, 114, 20
Millholland S. C., Spalding C., 2020, ApJ, 905, 71
Montalto M., 2023, MNRAS, 518, L31
Montalto M. et al., 2020, MNRAS, 498, 1726
Montalto M. et al., 2024, A&A, 687, A226
Morris R. L., Twicken J. D., Smith J. C., Clarke B. D., Jenkins J. M., Bryson S. T., Girouard F., Klaus T. C., 2020, in Jenkins J. M., ed., Kepler Data Processing Handbook: Photometric Analysis, Kepler Science Document KSCI-19081-003, id. 6. NASA Ames Research Center
Mortier A. et al., 2020, MNRAS, 499, 5004
Murgas F. et al., 2022, A&A, 668, A158
Mustill A. J., Lambrechts M., Davies M. B., 2022, A&A, 658, A199
NASA Exoplanet Archive, 2025, Planetary Systems Composite Parameters, available at: https://catcopy.ipac.caltech.edu/dois/doi.php?id=10.26133/NEA13
Newville M., Stensitzki T., Allen D. B., Ingargiola A., 2014, LMFIT: Non-Linear Least-Square Minimization and Curve-Fitting for Python, Version 0.8.0, Zenodo
Nidever D. L. et al., 2015, AJ, 150, 173
Nielsen J., Gent M. R., Bergemann M., Eitner P., Johansen A., 2023, A&A, 678, A74
Olmschenk G. et al., 2021, AJ, 161, 273
Osborn H. P. et al., 2023, MNRAS, 523, 3069
Owen J. E., Murray-Clay R., 2018, MNRAS, 480, 2206
Owen J. E., Schlichting H. E., 2024, MNRAS, 528, 1615
Pepe F. et al., 2000, in Iye M., Moorwood A. F., eds, Proc. SPIE Conf. Ser. Vol. 4008, Optical and IR Telescope Instrumentation and Detectors. SPIE, Bellingham, p. 582
Pepe F. et al., 2021, A&A, 645, A96
Persson C. M. et al., 2018, A&A, 618, A33
Peterson M. S. et al., 2018, AJ, 156, 188
Petigura E. A., Marcy G. W., Howard A. W., 2013, ApJ, 770, 69
Petrovich C., Deibert E., Wu Y., 2019, AJ, 157, 180
Piskunov N., Valenti J. A., 2017, A&A, 597, A16
Polanski A. S. et al., 2024, ApJS, 272, 32
Pollacco D. L. et al., 2006, PASP, 118, 1407
Pu B., Lai D., 2019, MNRAS, 488, 3568
Queloz D. et al., 2000, A&A, 354, 99
Rauer H. et al., 2025, Exp. Astron., 59, 26
Reddy B. E., Lambert D. L., Allende Prieto C., 2006, MNRAS, 367, 1329
Ricker G. R. et al., 2015, J. Astron. Telesc. Instrum. Syst., 1, 014003
Ryabchikova T., Piskunov N., Kurucz R. L., Stempels H. C., Heiter U., Pakhomov Y., Barklem P. S., 2015, Phys. Scr, 90, 054005
Sanchis-Ojeda R., Rappaport S., Winn J. N., Kotson M. C., Levine A., El Mellah I., 2014, ApJ, 787, 47
Santos N. C. et al., 2004, A&A, 426, L19
Santos N. C. et al., 2013, A&A, 556, A150
Scargle J. D., 1982, ApJ, 263, 835
Schanche N. et al., 2020, MNRAS, 499, 428
Schönrich R., Binney J., Dehnen W., 2010, MNRAS, 403, 1829
Shappee B. J. et al., 2014, ApJ, 788, 48
Shporer A. et al., 2020, ApJ, 890, L7
Silva A. M. et al., 2022, A&A, 663, A143
Skrutskie M. F. et al., 2006, AJ, 131, 1163
Smith J. C. et al., 2012, PASP, 124, 1000
Sneden C. A., 1973, PhD thesis, Univ. Texas, Austin
Sousa S. G., 2014, Determination of Atmospheric Parameters of B. Springer-Verlag, Berlin, p. 297
Sousa S. G., Santos N. C., Israelian G., Mayor M., Monteiro M. J. P. F. G., 2007, A&A, 469, 783
Sousa S. G. et al., 2008, A&A, 487, 373
Sousa S. G., Santos N. C., Adibekyan V., Delgado-Mena E., Israelian G., 2015, A&A, 577, A67
Sousa S. G. et al., 2021, A&A, 656, A53
Speagle J. S., 2020, MNRAS, 493, 3132
Steffen J. H., Shakespeare C., Royer R., Rice D., Vazan A., 2025, ApJ, 991, L33
Stumpe M. C. et al., 2012, PASP, 124, 985
Taylor M. B., 2005, in Shopbell P., Britton M., Ebert R., eds, ASP Conf. Ser. Vol. 347, Astronomical Data Analysis Software and Systems XIV. Astron. Soc. Pac., San Francisco, p. 29
Thiabaud A., Marboeuf U., Alibert Y., Leya I., Mezger K., 2015, A&A, 580, A30
Thompson S. E. et al., 2018, ApJS, 235, 38
Thygesen E. et al., 2023, AJ, 165, 155
Tian H.-J. et al., 2015, ApJ, 809, 145
Tokovinin A., 2018, PASP, 130, 035002
Tu P.-W., Xie J.-W., Chen D.-C., Zhou J.-L., 2025, Nat. Astron., 9, 995
Turner D. A. et al., 2025, preprint (arXiv:2506.20564)
Twicken J. D., Chandrasekaran H., Jenkins J. M., Gunter J. P., Girouard F., Klaus T. C., 2010a, in Radziwill N. M., Bridger A., eds, ASP Conf. Ser. Vol. 7740, Software and Cyberinfrastructure for Astronomy. Astron. Soc. Pac., San Francisco, p. 77401U
Twicken J. D., Clarke B. D., Bryson S. T., Tenenbaum P., Wu H., Jenkins J. M., Girouard F., Klaus T. C., 2010b, in Radziwill N. M., Bridger A., eds, ASP Conf. Ser. Vol. 7740, Software and Cyberinfrastructure for Astronomy. SPIE, Bellingham, p. 774023
Udry S. et al., 2019, A&A, 622, A37
Valenti J. A., Piskunov N., 1996, A&AS, 118, 595
Van Eylen V., Agentoft C., Lundkvist M. S., Kjeldsen H., Owen J. E., Fulton B. J., Petigura E., Snellen I., 2018, MNRAS, 479, 4786
Venturini J., Guilera O. M., Haldemann J., Ronco M. P., Mordasini C., 2020, A&A, 643, L1
Wang H. S., Lineweaver C. H., Ireland T. R., 2019a, Icarus, 328, 287
Wang H. S., Liu F., Ireland T. R., Brasser R., Yong D., Lineweaver C. H., 2019b, MNRAS, 482, 2222
Wheeler J. C., Sneden C., Truran Jr J. W., 1989, ARA&A, 27, 279
Wilson T. G. et al., 2022, MNRAS, 511, 1043
Winn J. N. et al., 2017, AJ, 154, 60
Winn J. N., Sanchis-Ojeda R., Rappaport S., 2018, New Astron. Rev., 83, 37
Wright E. L. et al., 2010, AJ, 140, 1868
Zeng L. et al., 2019, Proc. Natl. Acad. Sci., 116, 9723
Ziegler C., Tokovinin A., Briceño C., Mang J., Law N., Mann A. W., 2020, AJ, 159, 19

APPENDIX A: *TESS* PHOTOMETRY

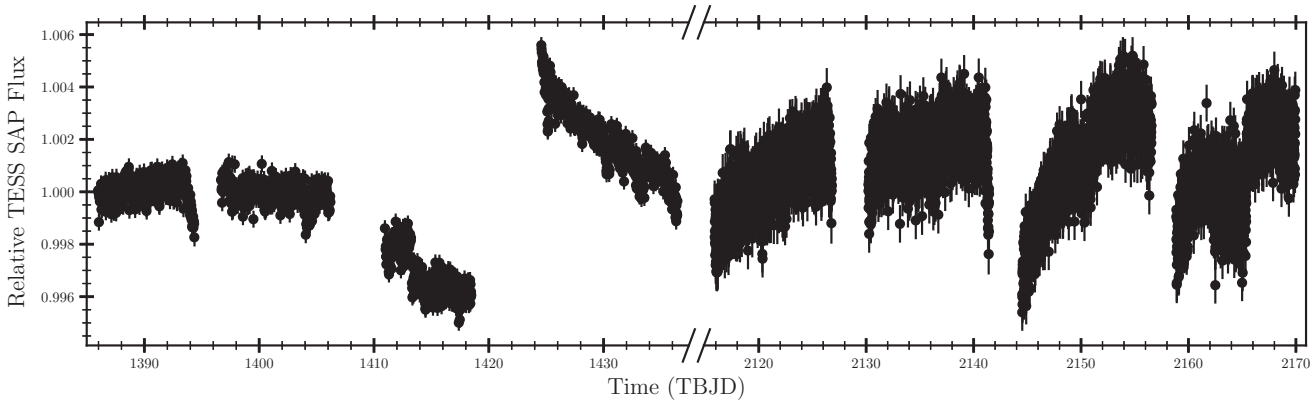

Figure A1. *TESS* SAP flux of TOI-2345 in sectors 3, 4, 30, and 31.

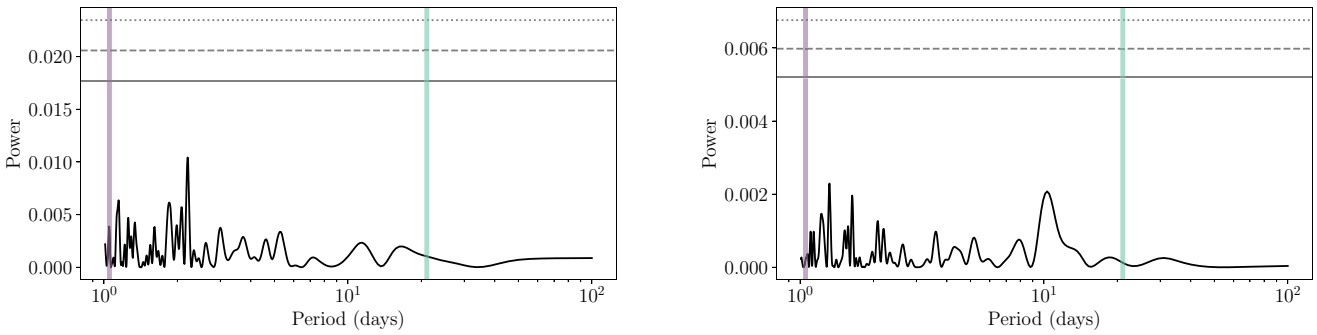

Figure A2. Lomb–Scargle periodogram of the available *TESS* data of sectors 3 and 4 (left) and sectors 30 and 31 (right). The orbital periods of TOI-2345 b and TOI-2345 c are shown by the purple and green line, respectively.

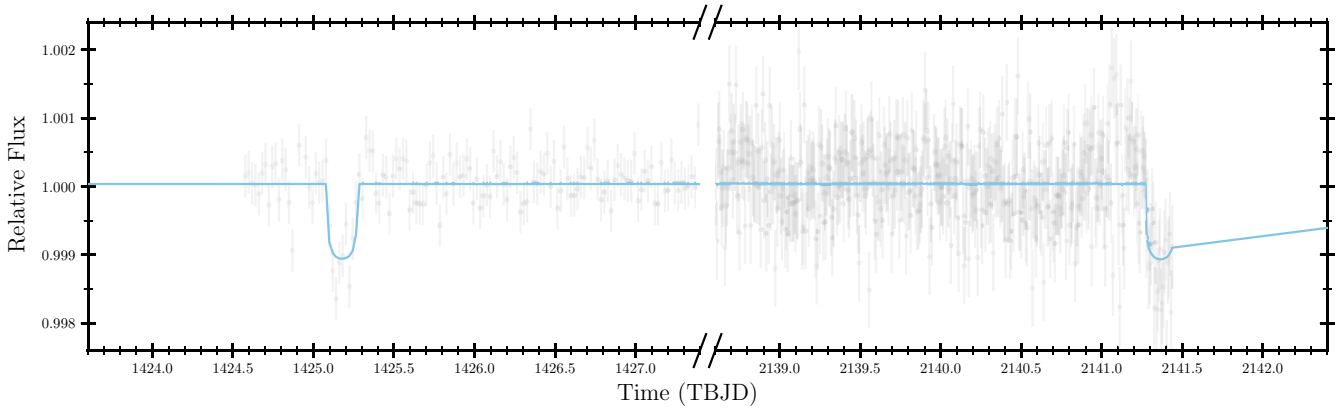

Figure A3. *TESS* photometry and our best-fitting model in juliet of the even transits of TOI-2345 c (transit 2 and 4) that are close to the sector gaps and were missed in the *TESS* vetting process. The signals of planet b are removed and the model is only showing planet c.

APPENDIX B: *CHEOPS* PHOTOMETRY

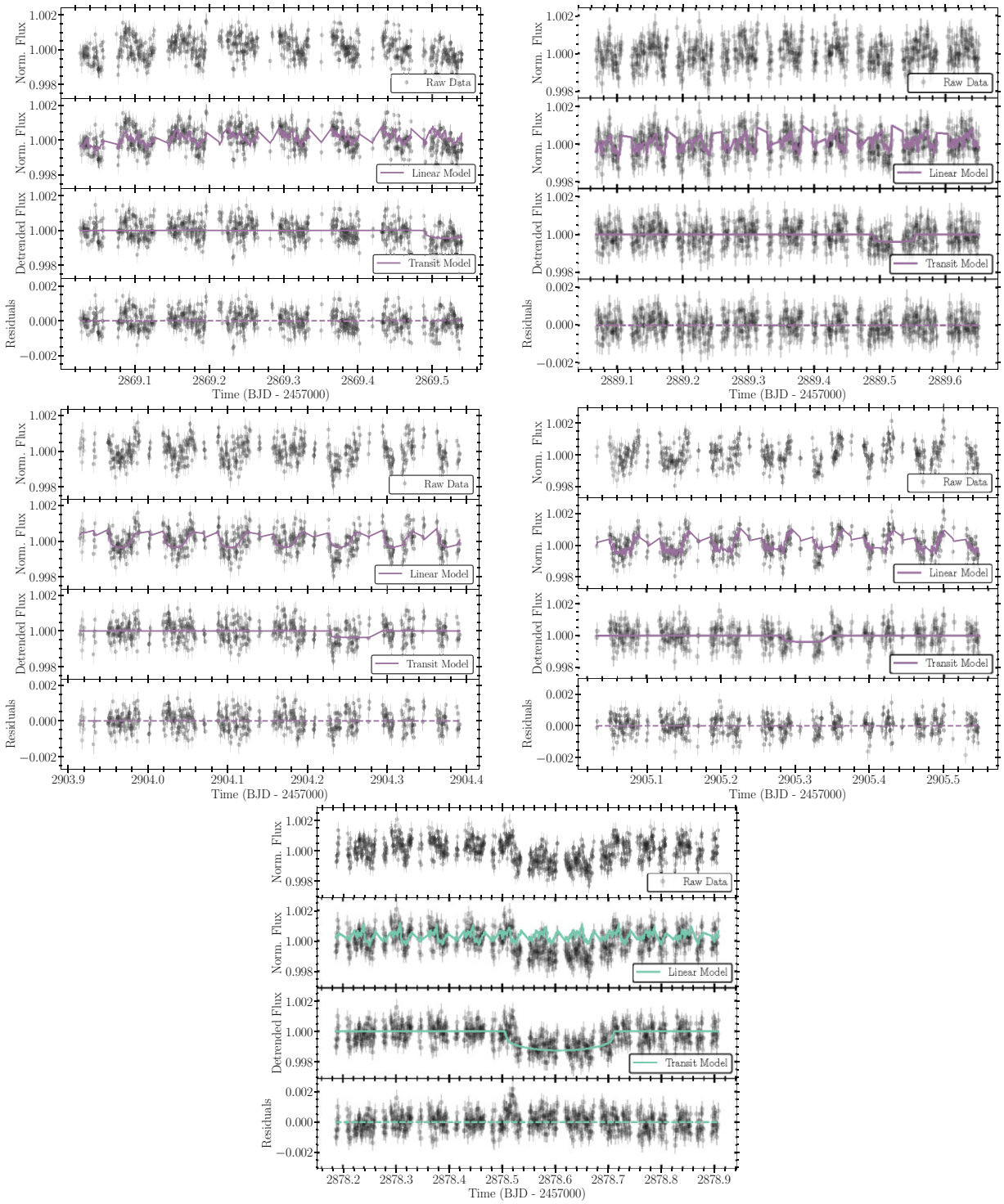

Figure B1. *CHEOPS* visits 1001, 1002, 3201, 3202 of planet b and 2401 of planet c and their detrending. The top row shows the data, the second row the linear model based on the selected detrending vectors, the third row shows the transit model and at the bottom the residuals of the fit are presented.

Table B1. Selected *CHEOPS* detrending vectors for DRP and PIPE of each visit. The detrending vectors are abbreviated as time (t), roll angle (ϕ), background (bg), and centroid offset (x, y).

Visit	Aperture (pixel)	DRP Detrending	PIPE Detrending
1	R16	bg, t, cosϕ	y, cos2ϕ, sin3ϕ, cos3ϕ
2	R17	bg, sinϕ, y^2, cosϕ, sin2ϕ, y, cos2ϕ	cos2ϕ, y, x^2, x, cos3ϕ
3	R17	bg, x, x^2	y, cos2ϕ, bg, x, cosϕ, sin3ϕ
4	R16	bg, t, sinϕ, x	sinϕ, cos2ϕ, bg cos3ϕ
5	R16	bg, x, sinϕ	sinϕ, y, sin3ϕ, cos2ϕ, x^2, t

APPENDIX C: HARPS RADIAL VELOCITIES

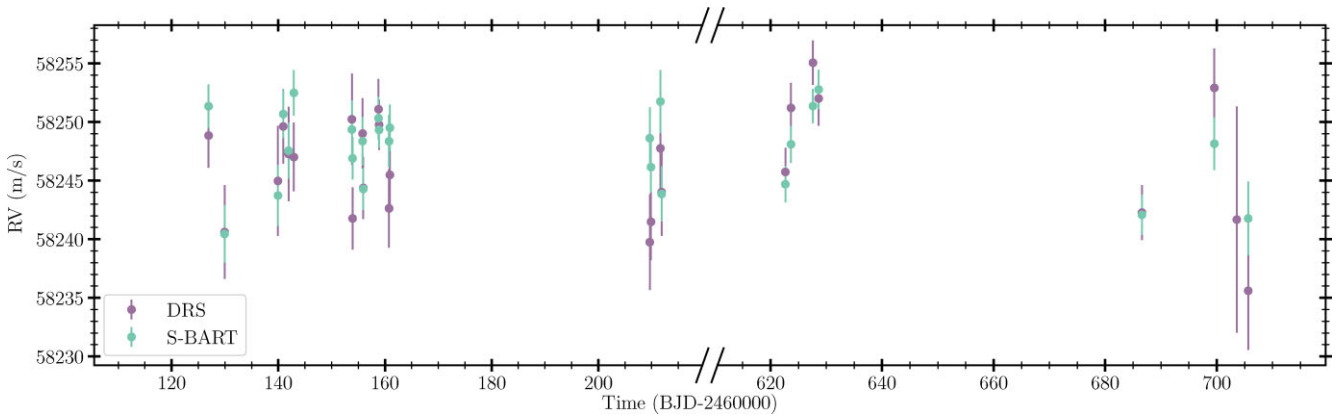

Figure C1. HARPS RVs as extracted from the DRS (purple) and S-BART (green) taken between 2023-07-01 and 2025-01-30.

Table C1. RVs from the HARPS DRS and the S-BART extraction.

Time (RJD)	DRS RV (m s^{-1})	$\sigma_{\text{DRS RV}}$ (m s^{-1})	S-BART RV (m s^{-1})	$\sigma_{\text{S-BART RV}}$ (m s^{-1})
60126.93	58248.8	2.8	58251.3	1.9
60129.92	58240.6	4.0	58240.4	2.4
60139.93	58245.0	4.7	58243.7	2.6
–	–	–	–	–

Table C2. Activity indicators from the HARPS DRS.

Time (RJD)	FWHM ($m\,s^{-1}$)	BIS ($m\,s^{-1}$)	Contrast	S-Index	Hα	Na	Ca
60126.93	6620.9 ± 5.5	-32.3 ± 5.5	65.877 ± 0.055	195.5 ± 4.3	0.25766 ± 0.00045	0.13288 ± 0.00031	0.1576 ± 0.0041
60129.92	6618.2 ± 8.0	-14.8 ± 8.0	66.166 ± 0.080	174.0 ± 7.1	0.25955 ± 0.00069	0.13122 ± 0.00046	0.1369 ± 0.0068
60139.93	6619.0 ± 9.4	-25.7 ± 9.5	65.888 ± 0.093	182.0 ± 7.9	0.25758 ± 0.00083	0.13309 ± 0.00056	0.1446 ± 0.0076
–	–	–	–	–	–	–	–

APPENDIX D: LONG-TERM PHOTOMETRY

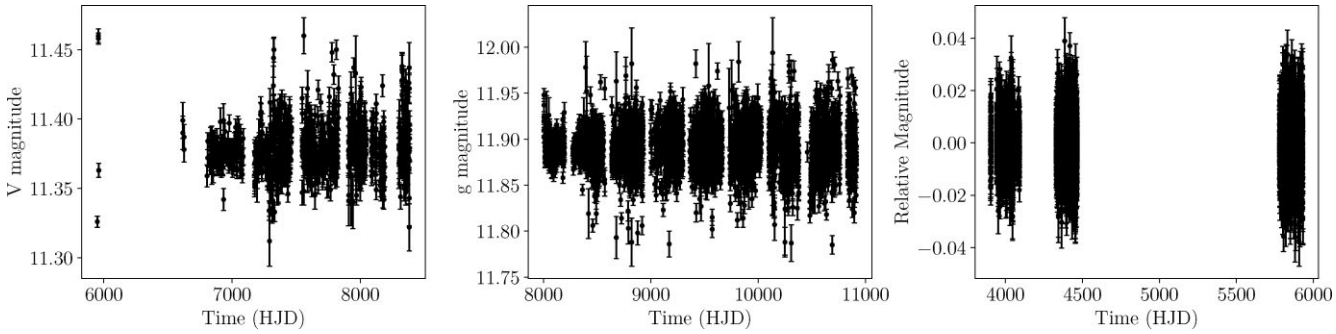

Figure D1. Light curves from ASAS-SN *V* band (left) and ASAS-SN *g* band (middle) and WASP (right) of TOI-2345.

APPENDIX E: PRIORS AND FITTED PARAMETERS

Table E1. Stellar and instrumental parameters of the joint fit in JULIET. Uniform distributions are noted by $\mathcal{U}$, normal distributions by $\mathcal{N}$ and log-uniform distributions by $\mathcal{L}$.

Parameter	Unit	Prior	Posterior
ρ_*	(kg/m^3)	$\mathcal{N}(2645, 142)$	2172^{+57}_{-63}
GP$_\rho$ *TESS*	(d)	$\mathcal{L}(0.001, 1000)$	21^{+291}_{-21}
GP$_\sigma$ *TESS*	(ppm)	$\mathcal{L}(0.000001, 1000000)$	$0.0000098^{+0.0000363}_{-0.0000069}$
q_1 *TESS*	–	$\mathcal{U}(0.0, 1.0)$	$0.31^{+0.19}_{-0.17}$
q_2 *TESS*	–	$\mathcal{U}(0.0, 1.0)$	$0.20^{+0.29}_{-0.14}$
q_1 *CHEOPS*	–	$\mathcal{U}(0.0, 1.0)$	$0.106^{+0.092}_{-0.058}$
q_2 *CHEOPS*	–	$\mathcal{U}(0.0, 1.0)$	$0.63^{+0.24}_{-0.30}$
jitter *TESS*	(ppm)	$\mathcal{L}(0.1, 1000)$	$3.57^{+31.28}_{-3.25}$
jitter *CHEOPS*	(ppm)	$\mathcal{L}(0.1, 100000)$	$193.60^{+21.58}_{-22.62}$
offset *TESS*	–	$\mathcal{N}(0, 0.1)$	$-0.0000337^{+0.0000061}_{-0.0000065}$
offset *CHEOPS*	–	$\mathcal{N}(0, 0.1)$	$0.000017^{+0.000010}_{-0.000010}$
jitter HARPS	(m s^{-1})	$\mathcal{L}(0.001, 100)$	$1.69^{+0.56}_{-0.52}$
offset HARPS	(m s^{-1})	$\mathcal{U}(58200, 59300)$	$58248.06^{+0.51}_{-0.49}$

[1]*Department of Physics, University of Warwick, Gibbet Hill Road, Coventry CV4 7AL, UK*
[2]*Space Research Institute, Austrian Academy of Sciences, Schmiedlstrasse 6, A-8042 Graz, Austria*
[3]*Department of Space, Earth and Environment, Chalmers University of Technology, Onsala Space Observatory, SE-439 92 Onsala, Sweden*
[4]*Instituto de Astrofisica e Ciencias do Espaco, Universidade do Porto, CAUP, Rua das Estrelas, P-4150-762 Porto, Portugal*
[5]*Observatoire astronomique de l'Université de Genève, Chemin Pegasi 51, CH-1290 Versoix, Switzerland*
[6]*Space Research and Planetary Sciences, Physics Institute, University of Bern, Gesellschaftsstrasse 6, CH-3012 Bern, Switzerland*
[7]*Center for Space and Habitability, University of Bern, Gesellschaftsstrasse 6, CH-3012 Bern, Switzerland*
[8]*Department of Astronomy, Stockholm University, AlbaNova University Center, SE-10691 Stockholm, Sweden*
[9]*Lund Observatory, Division of Astrophysics, Department of Physics, Lund University, Box 118, SE-221 00 Lund, Sweden*
[10]*ETH Zurich, Department of Physics, Wolfgang-Pauli-Strasse 2, CH-8093 Zurich, Switzerland*
[11]*CNRS, CNES, LAM, Aix Marseille Univ., 38 rue Frédéric Joliot-Curie, F-13388 Marseille, France*
[12]*Instituto de Astrofísica de Canarias, Vía Láctea s/n, E-38200 La Laguna, Tenerife, Spain*
[13]*Departamento de Astrofísica, Universidad de La Laguna, Astrofísico Francisco Sanchez s/n, E-38206 La Laguna, Tenerife, Spain*
[14]*Admatis, 5. Kandó Kálmán Street, 3534 Miskolc, Hungary*
[15]*Depto. de Astrofísica, Centro de Astrobiología (CSIC-INTA), ESAC campus, E-28692 Villanueva de la Cañada (Madrid), Spain*
[16]*Departamento de Fisica e Astronomia, Faculdade de Ciencias, Universidade do Porto, Rua do Campo Alegre, P-4169-007 Porto, Portugal*
[17]*INAF – Osservatorio Astronomico di Padova, Vicolo dell'Osservatorio 5, I-35122 Padova, Italy*
[18]*Institute of Space Research, German Aerospace Center (DLR), Rutherfordstrasse 2, D-12489 Berlin, Germany*
[19]*SETI Institute, Mountain View, CA 94043 USA/NASA Ames Research Center, Moffett Field, CA 94035, USA*
[20]*Centre for Exoplanet Science, SUPA School of Physics and Astronomy, University of St Andrews, North Haugh, St Andrews KY16 9SS, UK*
[21]*CFisUC, Departamento de Física, Universidade de Coimbra, P-3004-516 Coimbra, Portugal*
[22]*INAF – Osservatorio Astrofisico di Torino, Via Osservatorio, 20, I-10025 Pino Torinese To, Italy*
[23]*Centre for Mathematical Sciences, Lund University, Box 118, SE-221 00 Lund, Sweden*
[24]*ARTORG Center for Biomedical Engineering Research, University of Bern, 3008 Bern, Switzerland*
[25]*ELTE Gothard Astrophysical Observatory, 9700 Szombathely, Szent Imre h. u. 112, Hungary*
[26]*SRON Netherlands Institute for Space Research, Niels Bohrweg 4, NL-2333 CA Leiden, the Netherlands*
[27]*Centre Vie dans l'Univers, Faculté des sciences, Université de Genève, Quai Ernest-Ansermet 30, CH-1211 Genève 4, Switzerland*
[28]*Leiden Observatory, University of Leiden, PO Box 9513, NL-2300 RA Leiden, the Netherlands*
[29]*Dipartimento di Fisica, Università degli Studi di Torino, via Pietro Giuria 1, I-10125 Torino, Italy*
[30]*Department of Physics, National and Kapodistrian University of Athens, University Campus, Zografos GR-157 84 Athens, Greece*
[31]*Astrobiology Research Unit, Université de Liège, Allée du 6 Août 19C, B-4000 Liège, Belgium*
[32]*Kavli Institute for Astrophysics and Space Research, Massachusetts Institute of Technology, Cambridge, MA 02139, USA*
[33]*Department of Astrophysics, University of Vienna, Türkenschanzstrasse 17, A-1180 Vienna, Austria*
[34]*European Space Agency (ESA), European Space Research and Technology Centre (ESTEC), Keplerlaan 1, NL-2201 AZ Noordwijk, the Netherlands*
[35]*Institute for Theoretical Physics and Computational Physics, Graz University of Technology, Petersgasse 16, A-8010 Graz, Austria*
[36]*NASA Ames Research Center, Moffett Field, CA 94035, USA*
[37]*Konkoly Observatory, Research Centre for Astronomy and Earth Sciences, 1121 Budapest, Konkoly Thege Miklós út 15-17, Hungary*
[38]*Institute of Physics, ELTE Eötvös Loránd University, Pázmány Péter sétány 1/A, 1117 Budapest, Hungary*
[39]*IMCCE, UMR8028 CNRS, Observatoire de Paris, PSL Univ., Sorbonne Univ., 77 av. Denfert-Rochereau, F-75014 Paris, France*
[40]*Institut d'astrophysique de Paris, UMR7095 CNRS, Université Pierre & Marie Curie, 98bis blvd. Arago, F-75014 Paris, France*
[41]*Astrophysics Group, Lennard Jones Building, Keele University, Staffordshire ST5 5BG, UK*
[42]*European Space Agency, ESA - European Space Astronomy Centre, Camino Bajo del Castillo s/n, E-28692 Villanueva de la Cañada, Madrid, Spain*
[43]*INAF – Osservatorio Astrofisico di Catania, Via S. Sofia 78, I-95123 Catania, Italy*
[44]*Weltraumforschung und Planetologie, Physikalisches Institut, University of Bern, Gesellschaftsstrasse 6, CH-3012 Bern, Switzerland*
[45]*Dipartimento di Fisica e Astronomia 'Galileo Galilei', Università degli Studi di Padova, Vicolo dell'Osservatorio 3, I-35122 Padova, Italy*
[46]*Cavendish Laboratory, JJ Thomson Avenue, Cambridge CB3 0HE, UK*
[47]*German Aerospace Center (DLR), Markgrafenstrasse 37, D-10117 Berlin, Germany*
[48]*Institut fuer Geologische Wissenschaften, Freie Universitaet Berlin, Malteserstrasse 74-100, D-12249 Berlin, Germany*
[49]*Institut de Ciencies de l'Espai (ICE, CSIC), Campus UAB, Can Magrans s/n, E-08193 Bellaterra, Spain*
[50]*Institut d'Estudis Espacials de Catalunya (IEEC), E-08860 Castelldefels (Barcelona), Spain*
[51]*Space sciences, Technologies and Astrophysics Research (STAR) Institute, Université de Liège, Allée du 6 Août 19C, B-4000 Liège, Belgium*
[52]*HUN-REN-ELTE Exoplanet Research Group, Szent Imre h. u. 112., Szombathely H-9700, Hungary*
[53]*Leiden Observatory, University of Leiden, Einsteinweg 55, NL-2333 CA Leiden, the Netherlands*
[54]*Institute of Astronomy, University of Cambridge, Madingley Road, Cambridge CB3 0HA, UK*
[55]*Planetary Discoveries, Valencia, CA 91354, USA*
[56]*Department of Physics, Engineering and Astronomy, Stephen F. Austin State University, 1936 North St, Nacogdoches, TX 75962, USA*

This paper has been typeset from a TEX/LATEX file prepared by the author.